4-25-2011

The Double Galaxy Cluster Abell 2465 - I. Basic Properties: Optical Imaging and Spectroscopy

Gary A. Wegner
Dartmouth College

Monthly Notices
of the
ROYAL ASTRONOMICAL SOCIETY

Mon. Not. R. Astron. Soc. **413,** 1333–1352 (2011) doi:10.1111/j.1365-2966.2011.18218.x

The double galaxy cluster Abell 2465 – I. Basic properties: optical imaging and spectroscopy

Gary A. Wegner★

Department of Physics and Astronomy, Dartmouth College, 6127 Wilder Laboratory, Hanover, NH 03755, USA

Accepted 2010 December 16. Received 2010 December 15; in original form 2010 November 1

ABSTRACT

Optical imaging and spectroscopic observations of the $z = 0.245$ double galaxy cluster Abell 2465 are described. This object appears to be undergoing a major merger. It is a double X-ray source and is detected in the radio at 1.4 GHz. The purpose of this paper is to investigate signatures of the interaction of the two components. Redshifts were measured to determine velocity dispersions and virial radii of each component. The technique of fuzzy clustering was used to assign membership weights to the galaxies in each clump. Using redshifts of 93 cluster members within 1.4 Mpc of the subcluster centres, the virial masses of the north-east (NE) and south-west (SW) components are $M_{\rm v} = 4.1 \pm 0.8 \times 10^{14}$ and $3.8 \pm 0.8 \times 10^{14}\,{\rm M}_{\odot}$, respectively. These agree within the errors with masses from X-ray scaling relations. The projected velocity difference between the two subclusters is $205 \pm 149\,{\rm km\,s^{-1}}$. The anisotropy parameter, β, is found to be low for both components. Spectra of 37 per cent of the spectroscopically observed galaxies show emission lines and are predominantly star forming in the diagnostic diagram. No strong active galactic nucleus sources were found. The emission-line galaxies tend to lie between the two cluster centres with more near the SW clump. The luminosity functions of the two subclusters differ. The NE component is similar to many rich clusters, while the SW component has more faint galaxies. The NE clump's light profile follows a single Navarro–Frenk–White profile with $c = 10$ while the SW is better fitted with an extended outer region and a compact inner core, consistent with available X-ray data indicating that the SW clump has a cooling core. The observed differences and properties of the two components of Abell 2465 are interpreted to have been caused by a collision 2–4 Gyr ago, after which they have moved apart and are now near their apocentres, although the start of a merger remains a possibility. The number of emission-line galaxies gives weight to the idea that galaxy cluster collisions trigger star formation.

Key words: galaxies: clusters: general – galaxies: clusters: individual: Abell 2465.

1 INTRODUCTION

Fundamental questions of current astrophysics involve the roles of dark matter, baryonic matter and dark energy as driven by gravity in the formation of the large-scale structure and galaxies. Double or multiple galaxy clusters can potentially provide information on the dynamics and structure formation on ($r \gtrsim 1$ Mpc) scales, and interest in them has grown from both the standpoints of modelling and observation.

Although the presence of substructure in galaxy clusters has long been known, compared to single galaxy clusters, the properties of double and multiple clusters have received less attention owing to their added complexity. Interest in the observed substructure of galaxy clusters was pioneered by e.g. Geller & Beers (1982), and studies employing the radial infall model (Beers, Geller & Huchra 1982; Beers et al. 1991) were used for rough dynamical estimates.

With the realization of their importance, a growing number of systems have now been more fully studied dynamically, from weak lensing, and in X-rays. A partial list includes Abell 168 (Hallman & Markevitch 2004), Abell 399/401 (Sakelliou & Ponman 2004), Abell 520 (Girardi et al. 2008), Abell 521 (Ferrari et al. 2003), Cl0024+17 (Jee et al. 2007), the 'bullet cluster', 1E 0657−56 (Clowe et al. 2006), Abell 2146 (Russell et al. 2010), RXJ 1347.5−1145 (Bradač et al. 2008a), A399 and A401 (Yuan et al. 2005), Abell 2163 (Maurogordato et al. 2008), Abell 85 (Tanaka et al. 2010) and Abell 901/902 (Heiderman et al. 2009). Okabe & Umetsu (2008) studied seven merging clusters using weak lensing.

★E-mail: gaw@bellz.dartmouth.edu

Radio emission from merging clusters in the form of diffuse non-thermal radio haloes or relics that arise from merger shocks in the interactions of the colliding galaxy clusters has also been described by several groups including Slee et al. (2001) and Feretti (2002) who described several objects, Bagchi et al. (2006), Abell 3376; Orrú et al. (2007), Abell 2744 and Abell 2219; Bonafede et al. (2009), Abell 2345; and van Weeren et al. (2009), A2256. Skillman et al. (2010) summarized the modelling situation.

Modelling galaxy cluster mergers and collisions predicts observable signatures (e.g. Roettiger, Loken & Burns 1996, 1997; Ricker 1998; Takizawa 2000; Ricker & Sarazin 2001; Ritchie & Thomas 2002; Springel & Farrar 2007; Mastropietro & Burkert 2008; Poole et al. 2008; Planelles & Quilis 2009). These simulations have mostly focused on the behaviour of the baryonic and dark matter components and used a range of initial profiles and conditions and impact parameters which include both off-centre and head-on collisions. These calculations predict differing behaviours for the baryonic and dark matter components of the clusters at subsequent phases of the collisions. In a typical merger, the dark matter and the baryonic gas are elongated along the collision axis with a displacement between the baryonic and dark matter components. The gas, in addition, is shocked which results in multiple X-ray peaks and gas splashed perpendicularly to the direction of the merger. This produces non-isothermal temperature distributions, and the increased ram pressure from the shocks could induce star formation in the member galaxies as well as 'sloshing' (Markevitch & Vikhlinin 2007).

Several authors have attempted to extract information from double and multiple galaxy clusters on the nature of gravity and dark matter on galactic cluster ($\sim$1 Mpc) distance scales, and up to now this was mainly centred on analysing the 1E 0657−56 cluster. Farrar & Rosen (2006), Brownstein & Moffat (2007), Angus & McGaugh (2008), Schmidt, Vikhlinin & Hu (2009) and De Lorenci, Faundez-Abans & Pereira (2009) are among those who investigated whether modifications to gravity are needed to fit the available dynamical data. Springel & Farrar (2007), Pointecouteau & Silk (2005) and Hayashi & White (2006), however, indicated that modifications are unneccesary. For studying the properties of dark matter, the situation is somewhat more definite. Clowe et al. (2006) used weak lensing measurements of the bullet cluster to indicate direct proof of the presence of dark matter in the offset between the X-ray gas and the lensing centres. Shan et al. (2010) have studied further offsets between dark and ordinary matter in a further 38 lensed galaxy clusters. Galaxy clusters have been employed to place limits on neutrino masses (e.g. Tremaine & Gunn 1979; Natarajan & Zhao 2008; Angus, Famaey & Diaferio 2010) and to discuss whether or not such particle masses are needed to save the modified Newtonian dynamics formula.

Even if one dismisses such claims, a considerable amount of more conventional information is obtainable from double galaxy clusters. This includes possible modifications to luminosity functions (LFs), mass profiles and velocity dispersion anisotropy measures (the β parameter) as a result of their interactions. LFs contain information on the galaxy formation history (e.g. Bingelli, Sandage & Tammann 1988) and have been studied in detail at a range of redshifts and environments, mostly for single systems (e.g. Wilson et al. 1997; Blanton et al. 2003; Christlein & Zabludoff 2003; De Propis et al. 2004; Goto et al. 2005). Generally single and double Schechter functions (Schechter 1976), and Gaussian functions have been used to fit the LFs. Collisions may modify these properties compared to isolated single clusters at some level, but this question about the effects of merging in double galaxy clusters, i.e. whether or not their interactions produce or lower star formation along with AGN activity, has not been answered yet. Hwang & Lee (2009) have reviewed empirical and theoretical evidence for this and concluded that observations support the importance of mergers. Haines et al. (2009) and Chung (2010) have reported evidence of enhanced star formation rates in interacting clusters including the bullet cluster.

Mergers can distort galaxy cluster mass profiles. Many investigators have compared theoretical mass profiles with observations (e.g. Biviano & Girardi 2003; Katgert, Biviano & Mazure 2004; Pointecouteau, Arnaud & Pratt 2005; Kubo et al. 2007; Okabe & Umetsu 2008). Although not all details of these models are agreed upon, the Navarro–Frenk–White (NFW) profile (Navarro, Frenk & White 1997) fits most observed profiles within the virial radius with a concentration parameter c for galaxy clusters is in the range of $c = 4$–6 in agreement with theoretical results (e.g. Zhao et al. 2003). In addition, for a spherical system with the NFW profile, the anisotropy parameter $\beta = 1 - \sigma_\theta/\sigma_\mathrm{r}$ (where σ_θ is the azimuthal velocity dispersion and σ_r is the radial velocity dispersion) is predicted to be near 0 at the centre and to increase to about 0.3 beyond the virial radius and can provide information on the properties of the dark matter (Host 2009).

Many of the systems described in the literature are multiple and complex or minor mergers where the mass of one component is considerably larger than the other. The Abell 2465 double cluster discussed in this paper has a relatively uncomplicated substructure and shows some evidence for either a past collision or a commencing merger between the two components. The mean redshift is $z = 0.245$. *ROSAT* (Perlman et al. 2002), *XMM–Newton* (2008) data and redshifts show two physically related X-ray sources 5.5 arcmin (1.2 Mpc) apart [hereafter the north-east (NE) and south-west (SW) clumps]. As well, it is a 1.4-GHz radio source in the NRAO VLA Sky Survey (NVSS) (Condon et al. 1998). Both the virial and X-ray masses obtained in this paper indicate that the mass ratio of the two clumps is close to 1:1. Therefore, Abell 2465 is an example of a relatively rare major merger.

This paper surveys the optical properties of the Abell 2465 cluster and is organized as follows. Section 2 describes the new imaging and spectroscopy, Section 3 gives estimates from spectroscopy of virial masses and radii, and values of β and discusses available X-ray and radio data and emission-line galaxies in the two subclusters found from the spectra. Section 4 describes the determination of the LFs and Section 5 compares the estimates of the light profile and the corresponding mass profile. Section 6 discusses the results in relation to a collision and Section 7 lists the conclusions. The *Wilkinson Microwave Anisotropy Probe* (*WMAP*) 5-yr cosmological parameters are used throughout this paper.

2 OBSERVATIONS

Fig. 1 shows the central 8.1×8.1 arcmin^2 section of the i' Canada–France–Hawaii Telescope image described below, containing both clumps of Abell 2465 (SW and NE). Basic astronomical data are given in Table 1. The centres of the two clumps are separated by 5.5 arcmin.

2.1 Imaging data

The main part of the imaging data used in this paper is based on two sets of r' and i' images obtained by the quasi-stellar object (QSO) group of the CFHT in 2009. Five dithered r' images of 300-s exposure each were taken on 17 August at a mean airmass of 1.765, and five dithered i' images, each of 412 s, were observed on 23 August at a mean airmass of 1.36 using the Megaprime

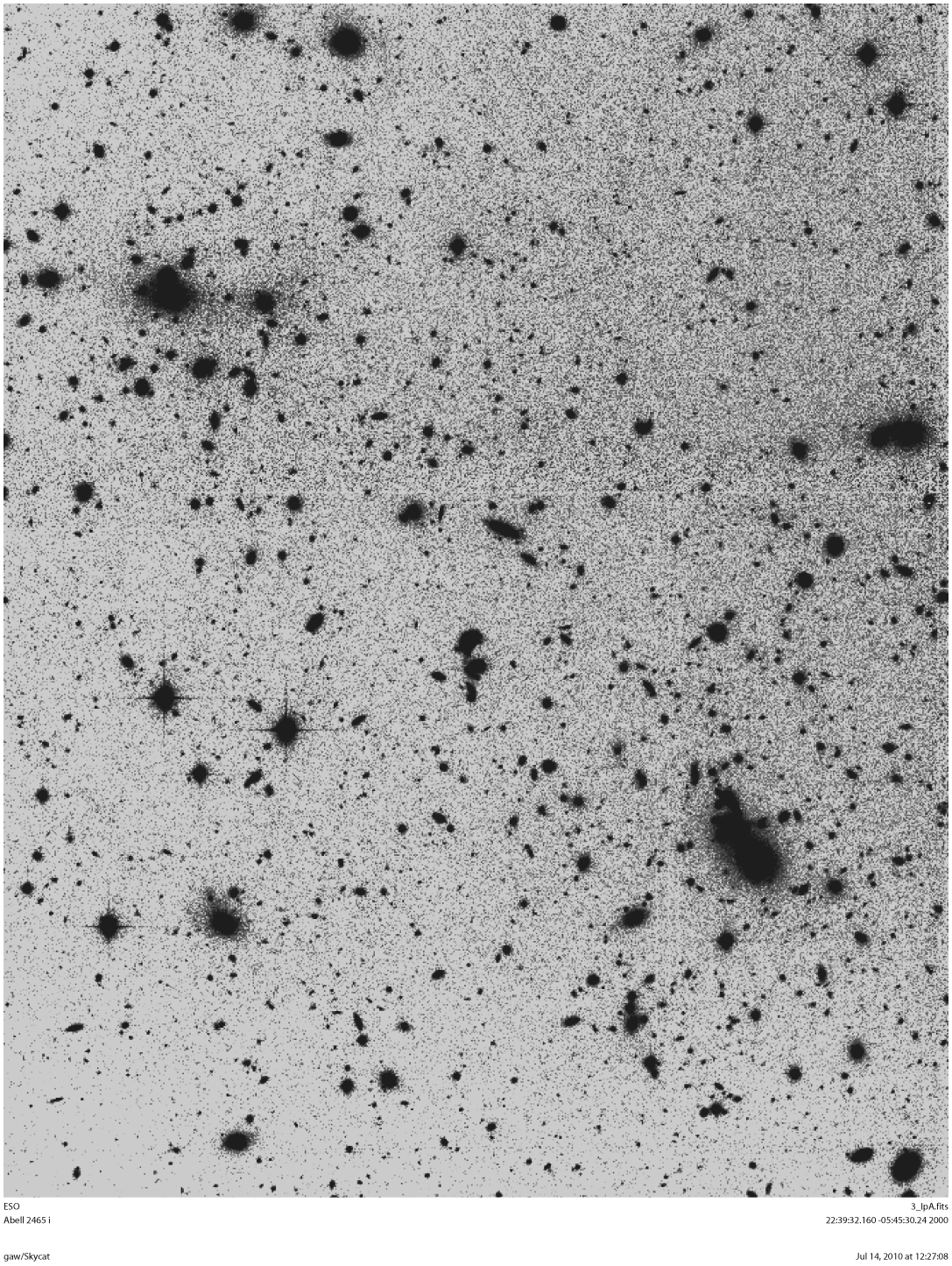

Figure 1. A portion of the combined CFHT i' Megaprime images of the centre of Abell 2465 showing the NE (upper left) and SW (lower right) clumps. The vertical edges of the picture are 8.1 arcmin in length. North is to the top and east is to the left-hand side (plot made using ESO's SkyCat, http://archive.eso.org/cms/tools-documentation/skycat).

instrument.[1] The ELIXER reductions of these images provided by the CFHT, which included bias subtraction and flattening, were employed and the photometric zero-points and extinctions provided for the run were used, although these were checked as explained below. The sets of dithered images were combined using the MSCRED programs in IRAF.[2] The task MSCFINDER was employed to put

[1] A description of this instrument including filters and ELIXER reductions can be found on the CFHT web page: http://ftp.cfht.hawaii.edu/Instruments/Imaging/MegaPrime/

[2] IRAF is distributed by the National Optical Astronomy Observatories, which are operated by the Association of Universities for Research in Astronomy, Inc., under cooperative agreement with the National Science Foundation.

Table 1. Basic data for Abell 2465 used in this paper.

(1)	(2)
NE *XMM–Newton* α_{J2000}	22 39 39.02
NE *XMM–Newton* δ_{J2000}	−05 43 28.2
SW *XMM–Newton* α_{J2000}	22 39 24.65
SW *XMM–Newton* δ_{J2000}	−05 47 15.0
NE BCG α_{J2000}	22 39 40.491
NE BCG δ_{J2000}	−05 43 26.75
SW BCG α_{J2000}	22 39 24.572
SW BCG δ_{J2000}	−05 47 17.37
Mean redshift z^a	0.2453 ± 0.0002
Luminosity distance[b]	1224 Mpc
Angular size distance[b]	791 Mpc
Distance modulus[b]	40.44 mag
Cosmology-corrected scale[b]	230.06 kpc arcmin^{-1}
Galactic extinction A_I [b]	0.077 mag
K-term $K_I(z)^c$	0.15 mag

[a]This paper, mean of 149 redshifts. [b]From NED using the *WMAP* 5-yr parameters. The NED is operated by the Jet Propulsion Laboratory, California Institute of Technology, under contract with the National Aeronautics and Space Administration. [c]Blanton & Roweis (2007) and Fukugita, Shimasaku & Ichikawa (1995).

coordinates to the WCS scale using the USNO-b catalogue. The program MSCIMAGE was used to make one single image from the 36 individual CCD images, and each of these was stacked to make a final r' and i' image with the task MSCSTACK. The resulting full width at half-maxima (FWHM) of stellar images in the vicinity of Abell 2465 are 0.81 and 0.47 arcsec for r' and i', respectively.

2.1.1 Photometry

The photometry of the images was measured using the SExtractor program (Bertin & Arnouts 1996; Holwerda 2005; Bertin 2009). The single image mode was first used to scan the i' image, which was secured in better seeing, to locate objects and the double image mode was secondly run for the r' image. The MAG_AUTO option and mostly default parameters recommended by Bertin (2009) for measurements of galaxies were set in the SExtractor. The colour zero-points and extinctions provided by the ELIXER processing were employed. These were checked for the brightest galaxies using CCD images of Abell 2465 obtained under photometric conditions from the 1.3-m telescope at the MDM Observatory in Arizona with Kron–Cousins R and I filters on the nights of 1995 November 18, 19 and 21 and 2009 October 15 and 16 and calibrated using Landolt (2009) with the result that $R = r' - 0.13 \pm 0.03$ and $I = i' - 0.61 \pm 0.05$. Jordi, Grebel & Ammon (2006) and Chionis & Gaskell (2008) gave comparable values within the errors for objects in the early-type galaxy colour range.

2.1.2 Star/galaxy separation

The SExtractor program provides the CLASS_STAR stellarity parameter $0 \leq s \leq 1$, whereby objects with $s \approx 1$ are stellar-like and $s \approx 0$ are galaxy-like. The s grows increasingly imprecise for faint sources due to seeing effects, so a better delineation between stars and galaxies is to employ the relation between MAG_AUTO, the Kron-like elliptical aperture magnitude, and MU_MAX, the peak surface brightness above background (Leauthaud et al. 2007; Penny et al. 2010). Fig. 2 plots objects in the i' image for which $s \geq 0.8$. The stellar locus and the outlined area used to determine which objects were stars are shown. If an object lies in this region and has $s \geq 0.8$, it is classed as a star.

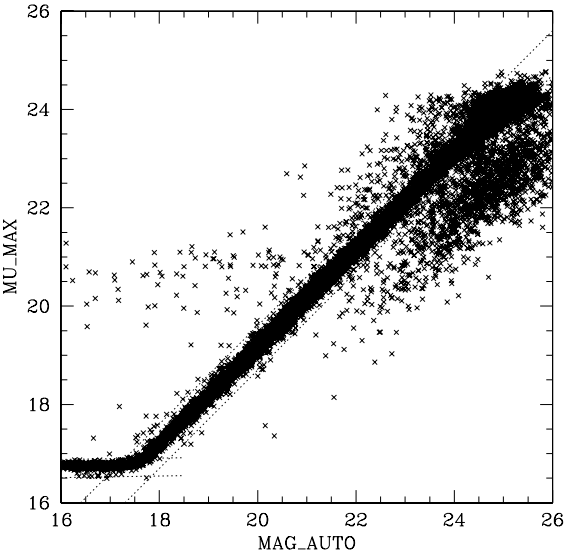

Figure 2. MU_MAX versus i' MAG_AUTO from SExtractor for stellar-like objects with $s > 0.8$ in the CFHT image. Dotted lines give the outlines of the region used to reject stars.

2.1.3 Red sequence

Using the objects classified as non-stellar or hence galaxies discussed above, the plot of i' against $(r' - i')$ colours centred on Abell 2465 shows a well-defined red sequence. Fig. 3 shows the magnitude–colour plot for the inner 18×12 arcmin^2 rectangle which contains the two subclusters. The red sequence is visible and

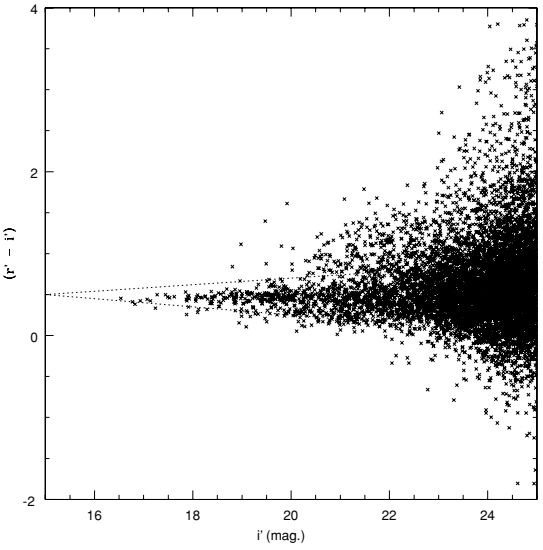

Figure 3. The red sequence for the objects classed as non-stellar in the inner 18×12 arcmin^2 central portion of the CFHT images. Dotted lines give the outlines of the region used to select red sequence cluster members.

the region used in the following is indicated. The chosen region extends to fainter magnitudes and is widened to account for the increasing magnitude errors.

2.2 Spectroscopic data

A more detailed dynamical analysis of Abell 2465 will be presented elsewhere as observations are still ongoing (Wegner et al., in preparation). Redshifts of galaxies centred on Abell 2465 were measured in 2007–2009 from the MDM Observatory and the Anglo-Australian Observatory (AAT) before the CFHT images were obtained. The target list was constructed using B and R CCD images from the MDM 1.3-m telescope of the inner 10 arcmin of the cluster and the superCosmos Sky Survey (SSS),[3] which is based on the UK Schmidt B_JRI photographic plates, to cover the entire 1 deg^2 centred on the cluster. Sources flagged as galaxies (i.e. CLASS = 1) were included. The zero-points of the SSS photographic photometry were adjusted using the CCD data, and sources with colour indices, $1.5 \leq (B_J - R_2) \leq 2.4$, which are centred on the red sequence, were included in the list.

Redshifts of 359 galaxies were obtained. Of these, 160 have redshifts in the range $70\,000 < cz < 77\,000\,\mathrm{km\,s^{-1}}$ which includes the cluster members. Of the remainder, 107 lie in the foreground and 92 lie behind the cluster. An additional 57 objects were stars and 93 targets did not have a high enough signal-to-noise ratio to secure a redshift.

The MDM observations were obtained with a long slit at the 2.4-m Hiltner telescope. The spectrograph was rotated in order to acquire multiple galaxies, ranging in number typically from three to 10 objects, simultaneously. In 2007 and 2009, the CCDS spectrograph with a 150 lines mm^{-1} grating was used. In 2007, the slit width was 1.3 arcsec and the wavelength covered was λλ4046–7245. In 2009, a 2.1-arcsec slit and a wavelength coverage of λλ4671–8591 were used. These set-ups yielded FWHM resolutions of 11 and 16 Å, measured from night sky lines. In 2008, the MKIII spectrograph, a 2.36-arcsec slit and a 300 lines mm^{-1} grism covering λλ4358–8716 were employed, yielding an FWHM resolution of 17 Å.[4] Three 20-min integrations were usually made with interspersed wavelength calibrations. Standard data reductions of the CCD spectra were carried out using IRAF, which includes bias subtraction, flat-fielding and wavelength calibration.

The largest number of redshifts was collected through the Service Observing Programme of the AAT with the AAOmega multi-object spectrograph in 2008 May 31 and July 25. Four 30-min exposures were obtained each night. The AAOmega simultaneously observes the blue and red portions of the spectrum. For the blue, the 580V grating which covers λλ3700–5800 was employed while for the red, the 385R grating that extends across λλ5600–8800 was used. The instrument nominally has 392 fibres of 2.0-arcsec diameter, and this set-up gives an FWHM resolution of about 6 Å. Wavelength calibration, flat-fields and biases were provided, and the preliminary reductions were facilitated using the 2DFDR program.[5] Subsequent reductions were done with IRAF.

Absorption-line measurements employed the Tonry & Davis (1979) cross-correlation method contained in the IRAF task fxcor. KIII stars were initially used for velocity standards with the MDM data, but for final reductions, the brightest cluster galaxies (BCGs) in Abell 2465 were used. These objects are shown in Table 2 at $\alpha_{J2000} = 339.852\,36$, 339.918 64 and 339.919 16. All spectra with $R < 3$ (Tonry & Davis 1979) and for which features could not be verified by eye were rejected.

Emission lines were used when an absorption-line measurement could not be obtained. If both emission and absorption velocities could be secured, they were averaged. The strong H and K lines of Ca II were also used as a check. A substantial number of galaxies had emission lines in their spectra that could be accurately measured and were used to verify the velocity scales of the AAT data. Compared to the imaging data, all spectra are of bright cluster members; the number of objects observed in the current set of spectra drops off rapidly fainter than $i' = 20$ which is a rough estimate of the limit of the current spectra.

Table 2 presents a subset of the redshift data for cluster members in the central regions of Abell 2465 which was used in this paper. Columns 1 and 2 are the galaxies' coordinates, Columns 3 and 4 are, respectively, the measured heliocentric redshift and its error, Column 5 gives the number of spectra, Column 6 states which telescope was used (A is for the AAT and M is for MDM), Column 7 is the i' magnitude from Section 2 and Columns 8 and 9 are the fuzzy weights explained in Section 3.1.

3 MASS ESTIMATES OF THE TWO CLUMPS

An estimate of the virial masses of the two clumps is made in the following. Although one can question the validity of this method, Poole et al. (2006) found that colliding clusters regain virial equilibrium relatively quickly. Takizawa, Nagino & Matsushita (2010) employed N-body simulations to compare virial mass estimates for colliding galaxy clusters and found that when the mass ratio is larger than 0.25, the estimated virial masses can be a factor of 2 too large, and in general, X-ray mass estimates are more accurate. While for the present, the question of virial equilibrium will be avoided, one should note that the virial masses found in Section 3.3 agree within their errors with those obtained from X-ray scaling relations.

3.1 Fuzzy clustering

A difficulty in dealing with galaxy clusters with overlapping components is the separation of the members of each sub-clump, when not all the phase space information can be known. For galaxy clusters with multiple components, this becomes a problem when it is necessary to resolve the members of the sub-clumps as in the present case of Abell 2465. This subject belongs to the wider realm of cluster analysis (e.g. Anderberg 1973; Höppner et al. 1999; Kaufman & Rousseeuw 2005; Gan, Ma & Wu 2007) and many authors have discussed solutions to the galaxy cluster problem, each with some success in their particular case, but at present, no single method is known to give a complete and secure solution. Pinkney et al. (1996) have reviewed several tests. Notable examples include the Δ-statistic (Dressler & Schechtman 1988), the DEDICA program of Ramella et al. (2007), and additional methods described in the papers of Salvador-Solé, Sanromà & González-Casado (1993), Tully (1980), Serna (1996) and Diaferio (1999). Tully (1980), Serna (1996) and Diaferio (1999) employed the single-link hierarchical clustering technique and constructed dendrograms. For the affinity parameter, Tully took the inverse of the attractive force, while Serna (1996) and Diaferio (1999) used the projected binding energy

[3] http://www-wfau.roe.ac.uk/sss/index.html

[4] Further details of these instruments can be found on the MDM Observatory web page: http://www.astro.lsa.umich.edu/obs/mdm/technical/index.html

[5] Descriptions of the AAOmega can be found at http://www.aao.gov.au/local/www/aaomega/

Table 2. Redshifts for cluster members in the central regions of Abell 2465 SW and NE.

α_{J2000}	δ_{J2000}	cz (km s^{-1})	εcz (km s^{-1})	N_{obs}	Tel.	i' (mag)	w_i (SW)	w_i (NE)
339.758 08	−5.794 50	72 990	29	1	A	19.231	0.6540	0.3450
339.781 49	−5.757 72	72 540	196	1	A	19.114	0.6790	0.3200
339.796 00	−5.796 44	73 972	37	1	M	18.894	0.7900	0.2090
339.796 96	−5.832 81	72 338	63	1	A	18.394	0.7280	0.2710
339.802 19	−5.784 19	73 571	177	1	M	19.456	0.8310	0.1690
339.808 87	−5.744 50	73 949	9	1	A	19.269	0.7130	0.2860
339.812 99	−5.750 97	72 992	35	1	M	18.626	0.7900	0.2090
339.816 62	−5.799 06	73 586	192	1	A	18.795	0.9170	0.0820
339.821 41	−5.708 61	73 235	139	1	M	19.976	0.5470	0.4520
339.824 28	−5.744 00	74 204	108	1	M	19.846	0.7180	0.2810
339.826 97	−5.742 89	74 196	45	1	M	19.094	0.7220	0.2780
339.834 84	−5.826 44	72 171	213	1	M	18.867	0.8000	0.1990
339.834 99	−5.739 75	74 032	115	1	A	19.031	0.7060	0.2940
339.835 24	−5.755 08	73 520	110	1	M	18.984	0.8800	0.1190
339.835 42	−5.822 69	72 566	10	1	A	17.138	0.9230	0.0760
339.840 21	−5.821 14	74 470	58	2	2M	18.410	0.8820	0.1170
339.840 76	−5.809 64	74 604	113	1	A	18.826	0.8850	0.1140
339.843 11	−5.752 19	72 357	150	1	M	18.301	0.8370	0.1620
339.843 38	−5.791 00	72 788	69	2	1A1M	18.886	1.0000	0.0000
339.846 62	−5.756 25	73 655	14	1	M	18.652	0.9140	0.0850
339.847 25	−5.861 58	72 244	125	1	M	18.225	0.7260	0.2730
339.847 38	−5.741 64	74 152	40	1	A	18.629	0.6980	0.3010
339.847 84	−5.812 22	73 476	30	1	M	17.460	1.0000	0.0000
339.850 04	−5.749 21	73 575	93	2	2M	19.577	0.7930	0.2060
339.852 36	−5.788 06	73 533	1	5	2A3M	16.534	1.0000	0.0000
339.852 91	−5.786 72	73 522	126	1	M	19.512	1.0000	0.0000
339.854 16	−5.784 44	72 242	14	2	2M	17.879	1.0000	0.0000
339.855 26	−5.783 58	72 094	171	1	M	18.061	1.0000	0.0000
339.856 26	−5.785 08	73 561	113	1	M	18.351	1.0000	0.0000
339.856 54	−5.780 22	73 429	30	1	M	18.370	1.0000	0.0000
339.856 69	−5.761 96	72 686	141	2	1A1M	18.528	0.9430	0.0560
339.857 96	−5.669 72	72 573	240	1	M	18.873	0.3360	0.6630
339.859 22	−5.778 11	72 956	242	1	A	19.912	0.9610	0.0380
339.864 32	−5.888 22	73 537	76	1	M	18.776	0.6480	0.3510
339.865 08	−5.738 89	73 976	24	1	A	20.007	0.5240	0.4750
339.866 09	−5.794 50	73 592	23	1	M	17.487	1.0000	0.0000
339.867 28	−5.765 81	72 014	40	1	A	18.565	0.8410	0.1580
339.873 32	−5.806 14	73 914	168	1	A	19.535	0.9330	0.0660
339.873 96	−5.762 78	74 040	147	1	M	19.918	0.7570	0.2420
339.874 62	−5.693 11	73 193	28	2	2A	19.127	0.1460	0.8530
339.880 04	−5.672 17	73 317	160	1	M	19.517	0.1810	0.8180
339.880 92	−5.750 26	74 626	158	1	A	17.853	0.5010	0.4980
339.882 97	−5.686 17	72 702	190	1	M	19.378	0.1810	0.8180
339.883 24	−5.682 25	73 647	36	1	M	18.848	0.1070	0.8920
339.884 64	−5.686 31	73 239	114	1	M	19.236	0.1010	0.8980
339.884 64	−5.766 03	73 244	8	1	M	18.565	0.7930	0.2060
339.884 83	−5.762 92	73 306	22	1	A	19.680	0.7460	0.2530
339.885 86	−5.689 11	73 326	42	1	M	21.910	0.1390	0.8600
339.888 46	−5.800 75	74 298	76	1	M	19.315	0.8170	0.1820
339.892 09	−5.806 78	73 395	7	1	M	20.391	0.8510	0.1490
339.894 20	−5.812 67	73 756	58	1	M	18.386	0.8430	0.1560
339.897 71	−5.805 97	74 019	45	1	A	19.407	0.7810	0.2180
339.898 68	−5.820 36	73 171	47	1	M	19.533	0.7860	0.2130
339.898 79	−5.695 12	75 000	74	3	1A2M	17.497	0.0070	0.9920
339.899 08	−5.826 53	74 029	44	1	M	20.867	0.7320	0.2670
339.899 58	−5.706 17	73 388	179	2	1A1M	18.445	0.0000	1.0000
339.900 45	−5.830 00	74 071	78	1	A	19.588	0.7190	0.2800
339.903 79	−5.756 11	73 388	130	1	M	18.578	0.3500	0.6490
339.904 79	−5.747 42	73 297	56	1	A	18.833	0.1950	0.8050
339.904 82	−5.677 11	75 208	54	1	A	18.703	0.1820	0.8170
339.905 21	−5.689 31	74 709	51	1	M	18.841	0.0830	0.9160
339.908 05	−5.724 61	73 311	126	1	M	18.090	0.0000	1.0000
339.909 17	−5.770 36	73 698	13	1	M	19.507	0.5080	0.4910
339.909 25	−5.778 28	74 085	35	1	A	19.569	0.5670	0.4320

Table 2 – *continued*

α_{J2000}	δ_{J2000}	cz (km s^{-1})	εcz (km s^{-1})	N_{obs}	Tel.	i' (mag)	w_i (SW)	w_i (NE)
339.909 76	−5.753 39	73 857	80	1	A	18.885	0.2480	0.7510
339.909 82	−5.734 39	73 220	185	1	M	20.117	0.0970	0.9020
339.910 43	−5.692 72	74 636	48	1	M	18.059	0.0020	0.9970
339.911 47	−5.819 64	72 128	64	1	A	17.652	0.7160	0.2830
339.911 83	−5.684 17	74 958	4	2	2M	18.740	0.1180	0.8810
339.911 87	−5.633 33	73 217	115	1	A	19.722	0.2760	0.7230
339.912 26	−5.834 36	72 025	40	1	A	20.034	0.6270	0.3720
339.912 93	−5.794 92	73 180	37	1	A	17.488	0.6930	0.3060
339.913 88	−5.737 89	73 060	23	1	M	18.805	0.0720	0.9270
339.914 03	−5.731 67	73 361	76	1	M	19.879	0.0030	0.9960
339.915 22	−5.732 14	72 576	40	3	3M	18.076	0.2090	0.7900
339.918 64	−5.723 89	73 044	31	3	1A2M	17.070	0.0000	1.0000
339.919 16	−5.721 81	74 061	119	2	2M	17.898	0.0000	1.0000
339.920 84	−5.731 89	74 847	76	1	M	19.318	0.1950	0.8040
339.922 03	−5.734 17	74 721	121	1	M	18.378	0.1010	0.8980
339.928 71	−5.740 33	73 186	93	1	M	18.394	0.0890	0.9100
339.928 99	−5.707 03	72 670	142	1	M	19.281	0.0450	0.9540
339.932 53	−5.721 94	72 745	74	2	1A1M	17.960	0.0000	1.0000
339.935 42	−5.670 39	73 467	131	1	M	19.377	0.1130	0.8860
339.938 96	−5.755 25	73 063	63	2	1A1M	19.138	0.2750	0.7240
339.940 89	−5.717 42	73 814	21	1	M	18.773	0.0240	0.9750
339.944 03	−5.653 08	74 188	150	1	M	18.526	0.2250	0.7740
339.945 28	−5.762 56	73 828	42	1	A	19.616	0.3020	0.6970
339.945 89	−5.644 14	74 096	264	1	M	20.321	0.3160	0.6830
339.947 91	−5.629 86	73 698	77	1	M	17.763	0.2930	0.7060
339.954 75	−5.791 49	73 571	138	3	2A1M	19.103	0.4570	0.5420
339.966 58	−5.756 61	73 555	46	1	A	17.582	0.2830	0.7160
339.966 89	−5.644 08	73 549	75	1	A	20.273	0.3160	0.6830
340.000 00	−5.738 03	73 528	11	1	A	18.061	0.3430	0.6560

between two galaxies, i and j:

$$E_{ij} = -G\frac{m_i m_j}{|r_i - r_j|} + \frac{1}{2}\frac{m_i m_j}{(m_i + m_j)}(v_i - v_j)^2, \quad (1)$$

where m_i, r_i and v_i are, respectively, the mass, position on the sky and the redshift for the ith galaxy.

The k-medoid method (KMM) has been employed by several investigators (e.g. Colless & Dunn 1996; Kriessler & Beers 1997; Yuan et al. 2005) to separate cluster members. Kriessler & Beers' KMM results compared favourably with previous analyses of 56 clusters. The KMM assigns each object uniquely to one cluster (Kaufman & Rousseeuw 2005), termed 'hard clustering', but given the observational errors and ambiguities of the data, it is unlikely that such a unique assignment is always accurate.

Consequently, the method of fuzzy analysis was explored to separate the cluster members of Abell 2465 (e.g. Sato, Sato & Jain 1997; Höppner et al. 1999; Kaufman & Rousseeuw 2005; Miyamoto, Ichihashi & Honda 2008). Fuzzy clustering generalizes the KMM and permits ambiguity in cluster membership by providing a 'membership coefficient', w_i, for each object, i, running from 0 per cent for a non-member to 100 per cent for a member of only one cluster. Assigning an object uniquely to a cluster by its largest membership coefficient (i.e. $w_i \geq 0.5$) returns the hard clustering result.

The fuzzy analysis algorithm (FANNY) and program of Kaufman & Rousseeuw (2005) were employed for the analysis of the cluster members. As in the above methods, one chooses the number of clusters k, an affinity between pairs of objects (i, j) and derives a dissimilarity matrix with elements $d(i, j)$. This was obtained by defining a projected binding energy:

$$b_{ij} = \frac{-m_i m_j}{|r_i - r_j|} + 1.162 \times 10^{-4}\mathcal{S}\frac{m_i m_j}{(m_i + m_j)}(v_i - v_j)^2, \quad (2)$$

using r_i in Mpc, v_i in km s^{-1} and m_i in units of 10^{12} M$_\odot$. A scaling factor, $\mathcal{S}$, was employed to lower the weight of the second term. The m_i were derived from the i' magnitudes of the galaxies using the formula of Cappellari et al. (2006) for the I band, $(M/L) = (2.35)(L_I/10^{10}\,\mathrm{L}_{I,\odot})^{0.32}$ and $I = i' - 0.61$. The b_{ij} were converted to dissimilarities using $d(i, j) = \frac{1}{2}[1 + \mathrm{erf}(\mathrm{b_{ij}}]$, which gives $0 \leq d(i,j) \leq 1$ whereby nearby and tightly bound pairs with large negative b_{ij} have small dissimilarities, and distant unrelated pairs are assigned positive dissimilarities.

Fig. 4 shows the resulting distribution of the galaxies in the two clumps and Fig. 5 shows histograms of their corresponding velocities. In this hard clustering presentation, the result is approximately what one intuitively expects as the galaxies are divided mostly into the two groups near the outlines of the circles in Fig. 4, and using the fuzzy weights in Fig. 5 the difference in the velocity peaks can be seen.

3.2 Virial masses

Virial masses were estimated from the redshift data following e.g. Carlberg et al. (1996) and Girardi et al. (1998). All quantities were referred to the rest frame of the clusters. A weighted virial mass estimator was used which reduces to the equation (4) of Heisler,

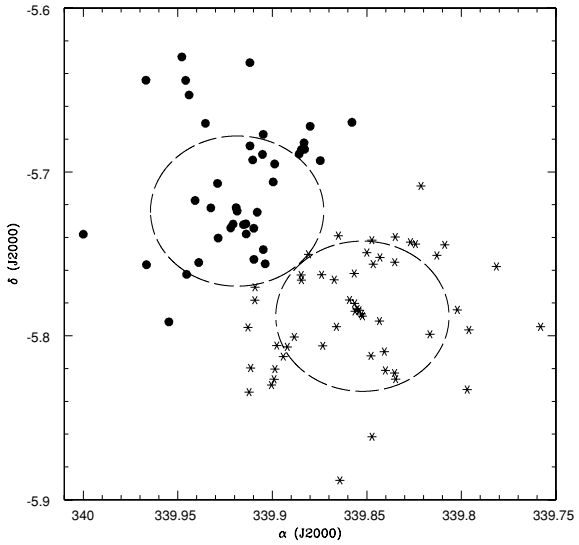

Figure 4. Distributions of the galaxies in Abell 2465 with measured redshifts and assigned to each clump using the hard clustering (i.e. membership coefficient, $w_i \geq 0.5$). Filled circles and asterisks denote the NE and SW clumps, respectively. The dashed circles are centred on the BCG of each clump near the X-ray centres and have radii of 2.75 arcmin or 0.63 Mpc which is half the distance between the two centres.

Tremaine & Bahcall (1985) for unit weights:

$$M_{\rm v} = \frac{3\pi \sum_i w_i}{2G} \frac{\sum_i w_i V_{zi}^2}{\sum_{i<j} w_i w_j / R_{\perp,ij}}, \quad (3)$$

where the w_i are the fuzzy clustering weights, $V_{zi} = (V_i - \bar{V})/(1+\bar{z})$ and $R_{\perp,ij}$ is the angular size distance between two galaxies i and j.

Galaxies within 1.4 Mpc of the clump centres and with redshift velocities $72\,000 < V_{zi} < 76\,000$ km s^{-1} were used to obtain $M_{\rm v}$. The galaxies and their redshifts, which were used, are given in Table 2.

For the NE clump, there are $\sum_i w_i = 49$ galaxies within this radius while for the SW clump, $\sum_i w_i = 44$. The resulting virial masses, $M_{\rm v}$, for NE and SW, respectively, are

$$4.1 \pm 0.8 \times 10^{14} \text{ and } 3.8 \pm 0.8 \times 10^{14}\,{\rm M}_\odot,$$

where the uncertainties are jackknife errors. Fig. 5 shows the histograms of the velocities. The corresponding mean redshifts for the two clumps are $\bar{V}_{\rm NE} = 73\,593 \pm 102$ km s^{-1} and $\bar{V}_{\rm SW} = 73\,388 \pm 109$ km s^{-1}, which yields a velocity difference of $\Delta V = 205 \pm 149$ km s^{-1}.

The virial radii, according to the formula $r_{200} = \frac{\sqrt{10}}{3}\frac{\sigma^2}{H(z)^2}$ (Carlberg et al. 1996), are 1.21 ± 0.11 Mpc (NE) and 1.24 ± 0.09 Mpc (SW). This assumes that the virial mass is approximated by $M_{200} = (4/3)\pi r_{200}^3 \Delta_{\rm c} \rho_o(z)$, where $\rho_o(z)$ is the critical density at redshift z and $\Delta_{\rm c}$ is the cluster's density enhancement, set equal to 200.

The masses of the two clumps calculated using the hard clustering weighting ($w_i = 0$ or 1) are 3.7 ± 0.7 and 3.0 ± 0.7 × 10^{14} M$_\odot$, respectively, for the SW and the NE clumps. For comparison, the redshift difference between the two BCGs near the centres of the NE and SW clumps is 489 km s^{-1}. The unweighted average of 149 cluster members inside 1° of the cluster centre is 73 530 ± 58 km s^{-1}.

A correction to $M_{\rm v}$ is required due to the whole cluster not being included in the calculation (e.g. Girardi et al. 1998, and references therein). This depends on the galaxy and velocity dispersion distributions with radius. A $c = 6$ NFW profile was assumed, and it was found that the correction could be neglected for the present data.

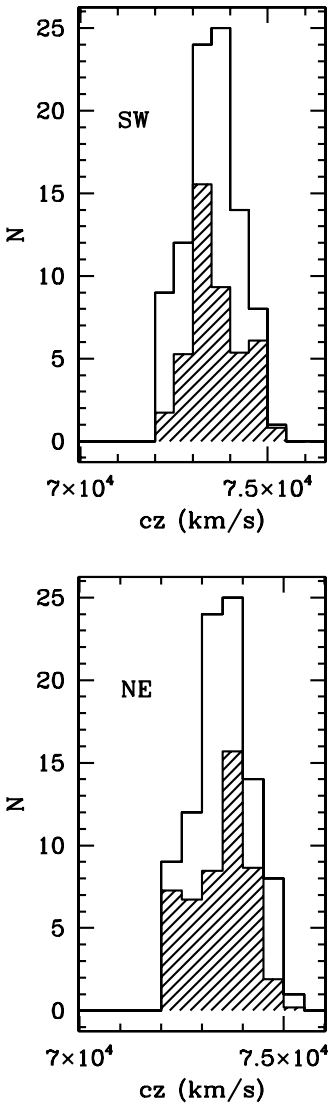

Figure 5. Histograms of redshifts of the two Abell 2465 clumps based on the fuzzy clustering. The upper unfilled histogram shows the whole sample. Lower shaded histograms show the weighted velocity distributions from the fuzzy weights that were used in determining the virial masses.

3.3 Comparison with X-ray masses

The virial masses can be compared with those from X-ray scaling relations. Both *ROSAT* and *XMM–Newton* observed Abell 2465 serendipitously. Contours of the *ROSAT* data are given in Perlman et al. (2002). Fig. 6 shows the *XMM–Newton* image alongside the 1.4-GHz radio data discussed in Section 3.4. Averaging the unabsorbed *ROSAT* values in the (0.5–2.0) keV band according to Vikhlinin et al. (1998) and Perlman et al. (2002) gives $f_{\rm X} = 3.605 \times 10^{-13}$ and 2.53×10^{-13} erg s^{-1} cm^{-2}, respectively, for the NE and SW clumps. The *XMM–Newton* values taken from the 2XMMi_DR3 catalogue in the (0.5–2.0) keV band are the ep_2 + ep_3 fluxes and are 2.44×10^{-13} and 2.08×10^{-13}, respectively. These were multiplied by 1.07 to correct for absorption, using $n_{\rm H} = 3.64 \times 10^{20}$ atoms cm^{-2} [the mean of the Kalberla et al. (2005) and Dickey & Lockman (1990) values implemented in HEASARC],

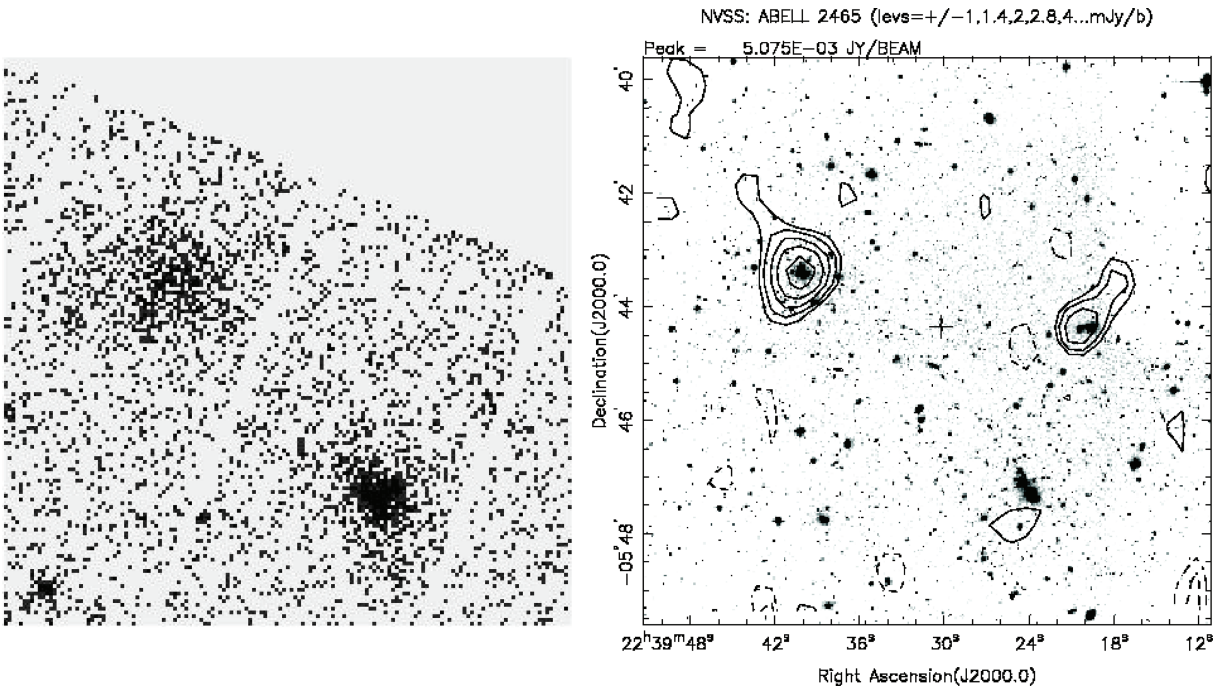

Figure 6. The X-ray and 1.4-GHz radio images of Abell 2465. Both are at the same scale. The vertical border of each box represents 2.3 Mpc at the distance of Abell 2465. North is at the top and east is to the left-hand side. Left-hand panel: 1–2 keV X-ray data near the cluster from a portion of archived *XMM–Newton* image 0149410401003 from project of PI S. Mathur. Right-hand panel: 1.4-GHz contours provided by the NVSS Postage Stamp Server superimposed on the i' image of this paper.

Wilms, Allen & McCray (2000) for the X-ray absorptivity per H atom in the interstellar medium and a 4-keV Raymond–Smith (Raymond & Smith 1977) 0.3 solar metals model at redshift $z = 0.245$.

Many authorities find scaling relations among X-ray luminosity, mass, temperature, etc. (e.g. Reiprich & Böhringer 2002; Popesso et al. 2005; Rykoff et al. 2008). The results of Popesso et al. (2005) for M_{200}, in the (0.1–2.4 keV) band, were adopted. A multiplicative factor of 1.60 was found to include the *ROSAT* and *XMM–Newton* (0.5–2.0) keV data into this band using the 4-keV Raymond–Smith model mentioned above. With the luminosity distance of 1224 Mpc for Abell 2465, $L_X = 8.94 \pm 1.44 \times 10^{43}$ erg s^{-1} for NE and $L_X = 6.84 \pm 0.43 \times 10^{43}$ erg s^{-1} for SW. The Popesso et al. (2005) uncorrected relation for mass, $\log M_{200} = [\log (L_X/10^{44}) + 1.15]/1.58$, yields

$$4.4 \pm 0.6 \times 10^{14} \text{ and } 3.6 \pm 0.2 \times 10^{14}\,\mathrm{M}_\odot$$

for the NE and SW clumps, respectively.

The L_X–T relation, $\log T_X = [\log (L_X/10^{44}) + 2.06]/3.30$ (Popesso et al. 2005), gives temperatures of

$$4.1 \pm 0.3 \text{ and } 3.75 \pm 0.2 \text{ keV},$$

for NE and SW, respectively, where the errors include the range in L_X and the scatter of the relation. The mass-weighted M_{200}–T_X relation found by Sanderson et al. (2003) gives nearly identical values of T_X.

Given T_X, the cooling times of the two clumps provide additional information. The bremsstrahlung cooling time for cluster gas of temperature T and hydrogen density n_p is

$$t_{\rm cool} = 8.5 \times 10^{10} \left(\frac{T}{10^8}\right)^{1/2} \left(\frac{n_{\rm p}}{10^{-3}\ \mathrm{cm}^{-3}}\right)^{-1} \quad (4)$$

(Sarazin 1986; equation 5.23). At the current temperature of $T \approx 4$ keV, n_p can be estimated from

$$\varepsilon = 3.0 \times 10^{-27} (T_g)^{1/2} n_{\rm p}^2 \quad (5)$$

(Sarazin 1986, equation 5.21). Using that $L/2 \approx \varepsilon\ (4/3)\pi r_c^3$ and the core radii $r_c = 42$ and 130 kpc for SW and NE (Vikhlinin et al. 1998), $t_{\rm cool} \approx 4$ and 20 Gyr for SW and NE, respectively. This indicates that SW is a cooling core (CC) cluster. This shorter $t_{\rm cool}$ in the SW subcluster results from its smaller r_c and is consistent with studies of CC clusters showing that they have core radii $r_c \lesssim 100$ kpc (e.g. Chen et al. 2007). As already noted, there is no evidence for strong AGN activity in either member of Abell 2465. It is tempting to identify the CC as a result of the cluster's merger, but O'Hara et al. (2006) argued that major mergers do not evolve CCs from their study of the scatter in scaling relations. However, Zu Hone & Markevitch (2009) found that 'sloshing' produced in mergers could be a source of heating in cluster cores.

3.4 Radio data

Abell 2465 appears to be detected in the 1.4-GHz NVSS (Condon et al. 1998). The radio contours are shown in Fig. 6 where they are superimposed on the i' image. A source with a peak flux of 6.2 ± 0.6 mJy falls near the NE component and appears to be a radio halo. A second elongated object with a peak flux of 3.1 ± 0.4 mJy is near the three early-type cluster members located about 3 arcmin north of the SW clump. No significant source lies in the SW optical component. If the two radio sources are at the distance of Abell 2465, their luminosities are 11×10^{23} and 6×10^{23} W Hz^{-1}, respectively. These are within the range of luminosity, temperature and size for diffuse radio haloes and relics summarized by Feretti (2002). The radio halo is centred near the NE subcluster which might identify it as the primary component of Abell 2465.

A more detailed analysis of the X-ray and radio data will be given elsewhere (Wegner & Johnson, in preparation).

3.5 Cluster velocity dispersion measurements

The run of radial velocity dispersion with radius contains information on the dynamics of the clusters. The results of measurements for the two clumps are shown in Fig. 7, where the fuzzy weighting was employed and errors given are jackknife errors.

The simplest case solves the spherical Jeans equation for the anisotropy parameter, β, where $\beta = 0$ for isotropic orbits and $\beta = 1$ is the non-physical limiting case of purely radial orbits. The aperture values of σ are shown in Fig. 7, where the formulae of Łokas & Mamon (2001) were used for the mean velocity dispersion inside an aperture of radius R:

$$\sigma_{\rm ap}^2(R) = \frac{S^2(R)}{M_{\rm p}(R)}, \tag{6}$$

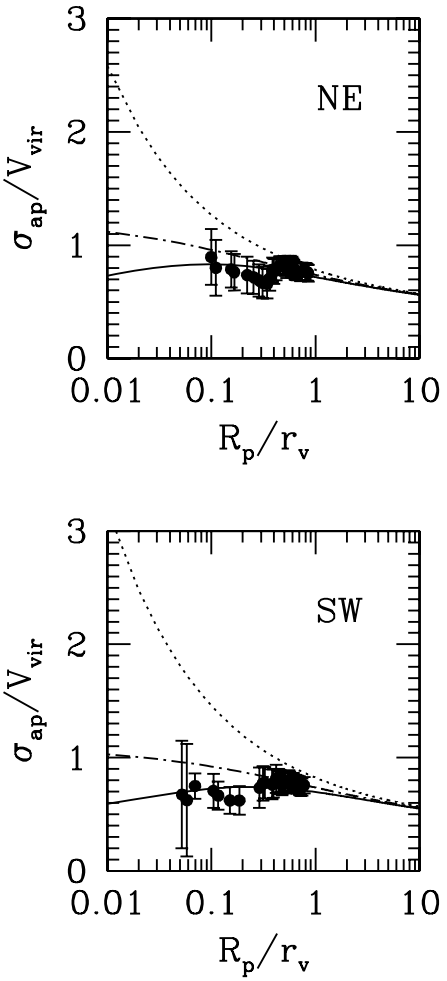

Figure 7. Radial profiles of the aperture-velocity dispersions for the two clumps in Abell 2465. The abscissae give the projected radial distances relative to the virial radius, $r_{\rm v}$, and the ordinates are the velocity dispersions and their errors relative to the circular velocity, $V_{\rm vir}$, defined in the text inside of $R_{\rm p}$. The different curves are for NFW models with $c = 10$ (SW) and $c = 4$ computed using Łokas & Mamon (2001). Dotted curve: $\beta = 1$, dot–dashed curve: $\beta = 0.5$ and solid curve: $\beta = 0$.

where $M_{\rm p}$ is described in equation (8) and S^2 is

$$S^2(R) = c^2 g(c) M_{\rm v} \left\{ \int_0^\infty \frac{\sigma_{\rm r}^2(s,\beta) s}{(1+cs)^2} \left(1 - \frac{2\beta}{3}\right) {\rm d}s + \int_R^\infty \frac{\sigma_{\rm r}^2(s,\beta)(s^2 - \tilde{R}^2)^{1/2}}{(1+cs)^2} \left[\frac{\beta(\tilde{R}^2 + 2s^2)}{3s^2} - 1\right] {\rm d}s \right\}, \tag{7}$$

where $s = r/r_{\rm v}$, $M_{\rm v} = (4/3)\pi r_{\rm v}^3 \Delta_{\rm c} \rho_o(z)$ is the virial mass and the other quantities are defined in Section 5. Łokas & Mamon (2001) gave analytical expressions for $\sigma_{\rm r}^2(s,\beta)/V_{\rm v}^2$ for constant $\beta = 0$, 0.5 and 1 and the Osipkov–Merritt (OM) model (Osipkov 1979; Merritt 1985), $\beta_{\rm OM} = s^2/(s^2 + s_a^2)$, which are used to evaluate the integral.

Fig. 7 compares curves for three values of β with the observed values in terms of the virial radius circular velocity $V_{\rm vir}^2 = GM_{\rm v}/r_{\rm v}$. OM models with $s_a \approx 4/3$ lie nearby the lower β curves and are not shown. Values of $V_{\rm vir}$ of 763 and 722 km s^{-1} were adopted for the NE and SW clumps, respectively. It can be seen that the most consistent anisotropy values are low, near $\beta = 0$, but agreement with $\beta = 1.0$ is ruled out for small radii. These values of $V_{\rm vir}$ place the data points on to the 0 and 0.5 β curves at the largest observed radii. Using the masses and radii found above, the corresponding values would be 1077 and 1043 km s^{-1}, but given the error in the value of $M_{\rm v}/r_{\rm v}$ which give $V_{\rm vir}$, these differ from the adopted values by less than 2 standard deviations.

The behaviour of β in the dark matter component of galaxy clusters has been investigated by several authors with the idea that this can probe its properties. For Λ cold dark matter (ΛCDM), Thomas et al. (1998) found that $\beta \leq 0.3$ inside the virial radius. Hansen & Piffaretti (2007) obtained similar values for two clusters as did Host (2009) and Host et al. (2009) for several X-ray clusters. The values of β for the subclusters of Abell 2465 are consistent with these results.

3.6 Emission-line galaxies in Abell 2465

Of the 149 galaxies in Abell 2465, observed spectroscopically with redshift $70\,000 \leq cz \leq 76\,000$ km s^{-1}, and within 1° of the cluster centres, 55, or 37 per cent, show detectable Hα emission of which 38 also have measurable [N II], Hβ and [O III] and can be plotted in the diagnostic diagram that separates star-forming galaxies, liners and AGNs. Equivalent widths were measured using the IRAF SPLOT routine and independently measured twice to estimate errors. The Hα and Hβ equivalent widths were adjusted for underlying absorption. Following Wegner & Grogin (2008), Hα was corrected by adding 2.32 Å to the measured emission and 2.02 Å was added to the Hβ emission, which are the absorption equivalent widths of these lines from galaxies that appear free of emission.

The resulting line ratios and their errors are given in Table 3, where Columns 1 and 2 are the coordinates of the galaxies. Columns 2–5 give the line ratio measurements and their errors. In Column 6, A and M denote whether AAT or MDM spectra were measured, and the last column is an estimated morphological type.

The morphological types of the emission-line galaxies were estimated from the i' image. The largest proportion of these appeared to be disturbed single objects without a visible companion. At least, 24 or 44 per cent have unusually asymmetrical discs or spiral arms. Only about six of these galaxies have obvious companions or tidal tails.

Table 3. Line ratio data for the emission-line galaxies shown in Fig. 8.

α_{J2000}	δ_{J2000}	log [N II]/Hα	ε log [N II]/Hα	log [O III]/Hβ	ε log [O III]/Hβ	Tel.	Type
339.453 46	−6.185 31	−0.499	0.021	−0.217	0.501	A	Sp
339.479 83	−6.202 42	−0.562	0.036	0.435	0.290	A	S0 pec
339.643 58	−5.613 42	−0.320	0.016	−0.173	0.460	A	Sa asy
339.646 12	−5.741 83	−0.353	0.012	0.049	0.251	A	S0 pec
339.653 78	−6.166 89	−0.077	0.018	0.091	0.264	A	S0
339.682 89	−5.837 81	−0.376	0.009	−0.410	0.193	A	S0 pec
339.683 62	−5.921 78	−0.631	0.038	0.419	0.318	A	S0
339.686 55	−5.888 31	−0.416	0.039	0.127	0.064	A	S0 asy+S0
339.692 40	−5.925 32	−0.671	0.036	0.205	0.122	2A	Sc
339.743 38	−5.945 25	−0.587	0.083	−0.038	0.011	A	Sp asy
339.751 80	−5.988 58	−0.297	0.003	0.238	0.315	A	SB0 rings
339.758 09	−5.794 50	−0.433	0.021	−0.370	0.108	A	Sa asy
339.763 82	−5.974 94	−0.356	0.036	0.215	0.229	A	SBc asy
339.787 41	−5.623 75	−0.785	0.003	0.542	0.179	A	Sp edge-on
339.808 87	−5.744 50	−0.482	0.001	0.576	0.442	A	Sa
339.815 14	−5.896 81	−0.368	0.089	0.417	0.017	MA	S0
339.826 57	−5.400 69	−0.390	0.033	0.252	0.528	A	Sa asy
339.837 68	−5.997 83	−0.594	0.054	0.389	0.322	A	S0 (POSS2)
339.843 26	−5.752 22	−0.339	0.047	0.070	0.236	A	SB0
339.850 74	−6.201 75	−1.309	0.111	0.720	0.051	A	Sc
339.856 63	−5.761 89	−0.256	0.001	−0.307	0.079	A	S0 asy
339.856 99	−5.892 56	−0.602	0.066	0.136	0.344	M	Sa
339.865 08	−5.738 89	−0.377	0.007	0.273	0.224	A	S0+companion
339.873 32	−5.806 14	−0.211	0.011	0.409	0.269	A	Sp asy
339.880 25	−5.562 44	−0.611	0.010	0.303	0.345	A	E+Sp
339.884 65	−5.686 19	−0.780	0.365	0.523	0.020	2M	Sp+E
339.884 83	−5.762 92	−0.297	0.013	0.018	0.326	A	SBc
339.885 86	−5.689 11	−0.912	0.074	0.303	0.298	M	E?
339.891 72	−5.601 64	−0.517	0.015	0.355	0.499	A	Sb pec
339.897 71	−5.805 97	−0.366	0.013	−0.135	0.053	A	Sp asy
339.900 45	−5.830 03	−0.325	0.018	0.535	0.267	M	S0
339.909 31	−5.778 29	−0.703	0.073	0.283	0.165	AM	Sp tail
339.944 37	−5.653 39	−0.534	0.016	0.200	0.377	M	S0 pec
339.945 28	−5.762 56	−0.233	0.053	0.158	0.039	A	Sp asy
340.063 08	−5.583 47	−0.485	0.068	−0.334	0.041	A	Sb asy
340.065 16	−5.621 83	−0.465	0.002	0.045	0.011	A	Sa asy
340.108 55	−5.574 39	−0.497	0.015	0.434	0.382	A	Sa asy
340.121 49	−5.953 19	−0.366	0.002	−0.494	0.033	A	Sb asy

Note: asy – one side of object noticeably stronger; pec – disturbed and/or shells.

The positions of the galaxies that have detected Hα emission, but the other emission lines are too faint to place them in the diagnostic diagram, are listed in Table 4 along with their morphologies.

Fig. 8 shows the diagnostic diagram. The line separating the Seyfert and liner regions is that given in Yan et al. (2006). The solid and dashed curves demarcating the edge of the star-forming region are from Kewley et al. (2001) and Kaufmann et al. (2003), respectively. The emission-line galaxies in Abell 2465 are nearly all star-forming objects. Only four objects lie on the border of the liner or Seyfert region. There are no no definite Seyferts or AGN activity dominating either clump.

The emission-line galaxies prefer to sit between the two subclusters with more near the SW clump. In Fig. 9, the left-hand panel shows the positions of all spectroscopically verified cluster members. The right-hand panel plots only emission-line objects and is an enlargement of the centre. The X-ray centres from Table 1 are indicated as crosses. The line passing through the centres approximates the cluster's axis, and the lines labelled A, B and C define stripes running perpendicular to this axis. The line B marks the distance half-way between the two subcluster centres. Using this centre line, of the 39 galaxies in the figure, 24 are on the SW side and 15 are on the NE side. However, the asymmetry is stronger in the central region of the cluster. In strip BC, 13 emission galaxies lie close to the SW centre while only five are near the NE clump in strip AB. For non-emission-line galaxies, the corresponding numbers are 20 and 15 galaxies, respectively.

This impression of asymmetry between the emission-line and non-emission-line galaxy distributions was tested with the two-dimensional Kolmogorov–Smirnov (KS) test (Fasano & Franceschini 1987; Lopes, Reid & Hobson 2007). Using the KS2D2S program (Press et al. 1992) for the two-sample test to compare the emission and non-emission samples indicates weakly that the two types of galaxies are slightly different at the 78 per cent significance level.

There are more emission-line galaxies near the centre of Abell 2465 than expected for single galaxy clusters. Balogh et al. (2004) and Rines et al. (2005) found an inverse correlation between the number of emission-line galaxies and density in galaxy clusters. For their composite cluster, Rines et al. (2005; fig. 2) found that the fraction of galaxies showing emission lines grows from 0 at the centre to 0.12 at $R_p = 0.5R_{200}$ with a mean near 0.06. For Abell 2465, the numbers of galaxies with observed spectra within the circles in

Table 4. Additional galaxies with detected Hα emission.

α_{J2000}	δ_{J2000}	Tel.	Type
339.588 28	−5.931 92	A	E
339.761 29	−5.871 31	A	S0 pec
339.795 99	−5.796 44	M	Sp tail
339.820 37	−5.858 08	M	S0 asy
339.847 38	−5.741 64	A	E
339.855 10	−5.781 22	M	SBc asy
339.867 31	−5.765 81	A	E
339.882 93	−5.686 17	M	S0
339.884 61	−5.766 03	M	S0
339.888 42	−5.800 75	M	S0
339.904 84	−5.747 22	A	S0
339.920 83	−5.731 92	M	E
339.935 24	−5.670 08	A	S0
339.938 99	−5.674 08	M	Sa
339.948 91	−5.625 42	M	E
340.109 77	−5.804 97	A	Sp

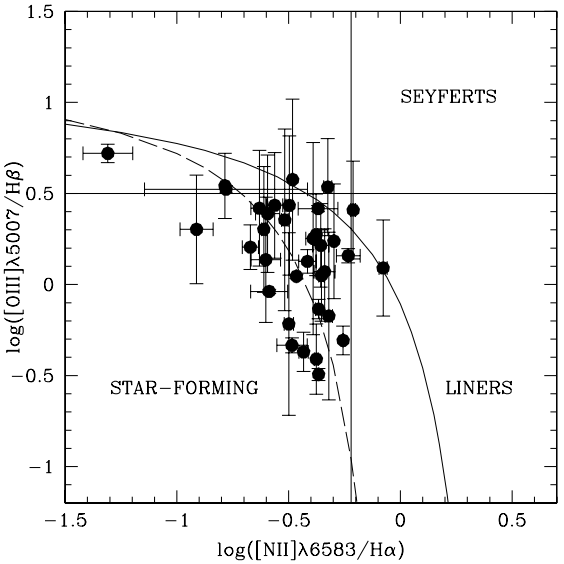

Figure 8. The diagnostic diagram for the emission-line galaxies in Fig. 9.

Fig. 4, which are projected radii of $R_p = 0.53R_{200}$ (0.63 Mpc) from the subcluster centres, are 27 and 22 for SW and NE, respectively. The corresponding numbers of emission-line galaxies are nine and four giving fractions of emission-line galaxies within these circles equal to 0.33 and 0.18. Even allowing for infall interlopers, these fractions appear different for Abell 2465 and the other clusters.

One question is whether the high fraction of star-forming galaxies could be due to a bias in selecting more emission-line galaxies because it is easier to obtain their redshifts. With the current data, this can be answered only roughly given the broad selection criteria and the employment of different spectroscopic instruments. A lower limit to the emission fraction can be estimated using the numbers in Section 2.2. First, 199/359 = 0.55 of the galaxies with redshifts should be cluster members. Secondly, if all 93 failed redshift targets are non-emission galaxies, 55 per cent or 51 would be cluster members. Thirdly, adding this to the number of observed cluster galaxies gives the lower limit to the fraction of star-forming cluster members to be 55/(149+51), or 28 per cent. This is still in excess of the fraction, with the mean being near 6 per cent for single clusters discussed above.

4 LUMINOSITY FUNCTIONS OF THE CLUMPS

In this paper, the statistical method of measuring all the galaxy photometry in the field and then subtracting the contribution of the background is employed using the nearly 1 deg^2 CFHT images. The photometry of the cluster is confined to the inner 22.4 × 18.0 arcmin^2 portion of the images and the sky background is estimated from the outer part of the images. The data provided by the program SExtractor (Bertin & Arnouts 1996; Holwerda 2005; Bertin 2009) described above were employed for separating stars and galaxies. The red sequence of the cluster described in Section 2.1.3 was used to find the cluster members.

4.1 Background galaxy determination

The background, its errors and the incompleteness were estimated in two steps. First, the resulting catalogue of galaxies was binned in magnitude using no colour cut. The outer portion of the CFHT i' image was binned in 1-mag intervals running from $i' = 16.0$ to 26.0. The total area used was 3069 arcmin^2. The number of detected objects and their colours was 89 579. The resulting number counts of the background along with their $\sqrt{N}$ errors are shown in Fig. 10, where they are compared to the number counts given by McCracken et al. (2001) from deeper CFHT i' imaging and Wilson (2003) who used Cousins I-band data from the same telescope.

These data agree well for $19 \lesssim i' \lesssim 23$. For i' brighter than 19, small number statistics dominate and it is assumed that the numbers of detections are complete. For i' fainter than 23, the completeness is estimated by taking the ratio of the present measurements to the McCracken et al. (2001) relation. The resulting estimate of completeness is also shown in Fig. 10 and is 1.0 for $i' = 17$–22. For fainter sources, it drops and this relation was adopted for the completeness.

The second step was to apply the same colour cut found for the red sequence to the background data. In addition to counting errors, there are the effects of cosmic variance in the background. To estimate these, the background was divided into four subsections of average 771 arcmin^2. The variance of these measurements was used to estimate the error in the background.

4.2 Luminosity functions of the two cluster centres

The LFs of the SW and NE clumps of Abell 2465 differ. They were obtained for the circular regions within 2.75 arcmin of the cluster centres as defined in Table 1. Identical colour cuts and the same background subtraction were applied to the data of both clusters. The magnitudes M_I are converted to luminosity using $L_I = 10^{-0.4(M_I - \mathrm{I}_\odot)}$ where $\mathrm{I}_\odot = 4.08$ (Binney & Merrifield 1998) and $M_I = i' + DM - A_I - K_I(z)$, using the data in Table 1. Bins fainter than $i' = 25$ were rejected due to the large incompleteness correction. The results shown in Fig. 11, where the error bars include both background and counting errors, show a significant difference between the two clumps, although both are within the range of LFs found for different clusters.

The bright portions of the two LFs are similar, but the SW clump has a substantially larger number of galaxies fainter than $M_I \approx -21$. This can also be seen by visual inspection of the central regions of the two clumps.

Although this statistical method provides a relative measure of the LFs of the two clumps, it is less secure than using redshift-based LFs. A possible explanation of the differing LFs of the two clumps might be that a distant cluster lies behind the SW clump. Fig. 12

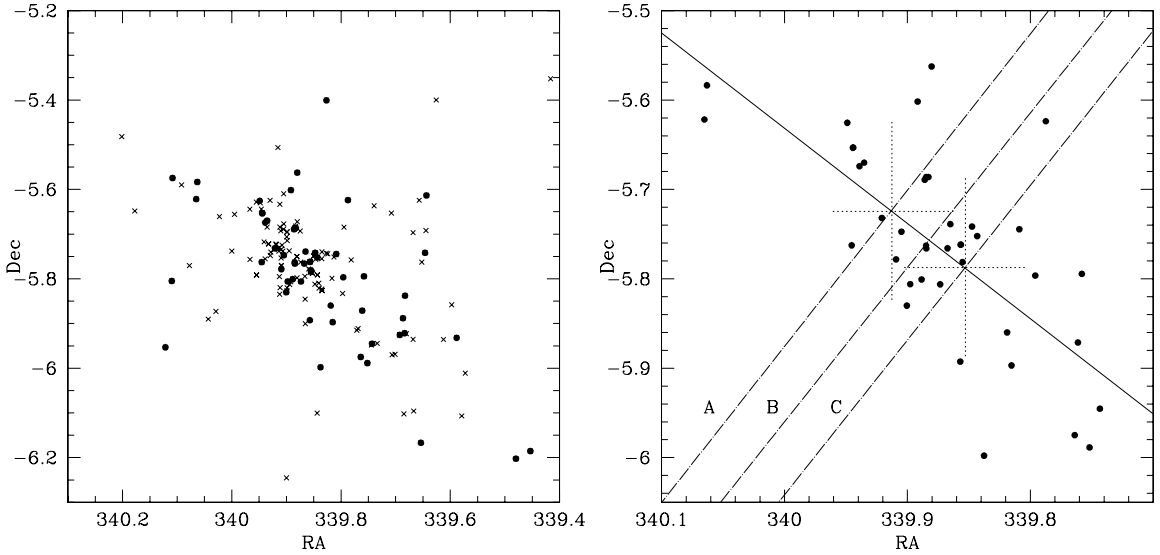

Figure 9. Left-hand panel: positions of emission-line (solid dots) galaxies with detected Hα emission and non-emission-line (crosses) galaxies observed in Abell 2465 with $70\,000 \leq cz \leq 76\,000\,\mathrm{km\,s^{-1}}$. Right-hand panel: positions of emission-line galaxies only, enlarged to show the central portion of the double cluster. The *XMM–Newton* positions of the two X-ray clumps are marked with the crosses.

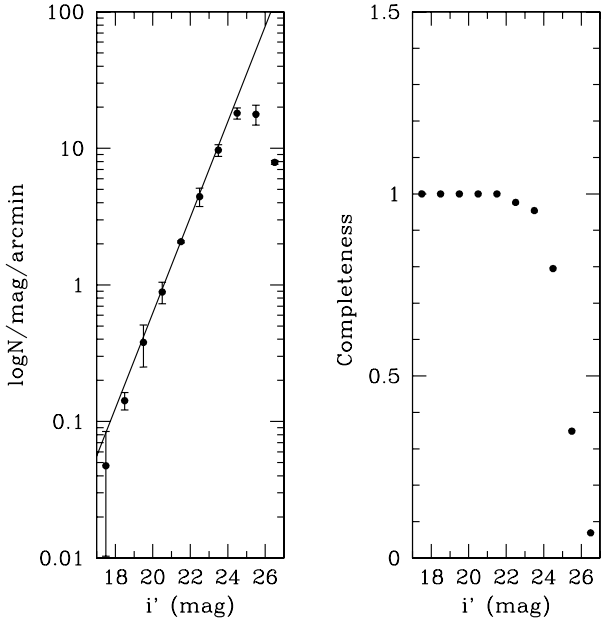

Figure 10. Left-hand panel: comparison of i'-band number counts found in this study with McCracken et al. (2001) deeper counts shown as the line. Right-hand panel: adopted i' completeness function for the galaxy number counts.

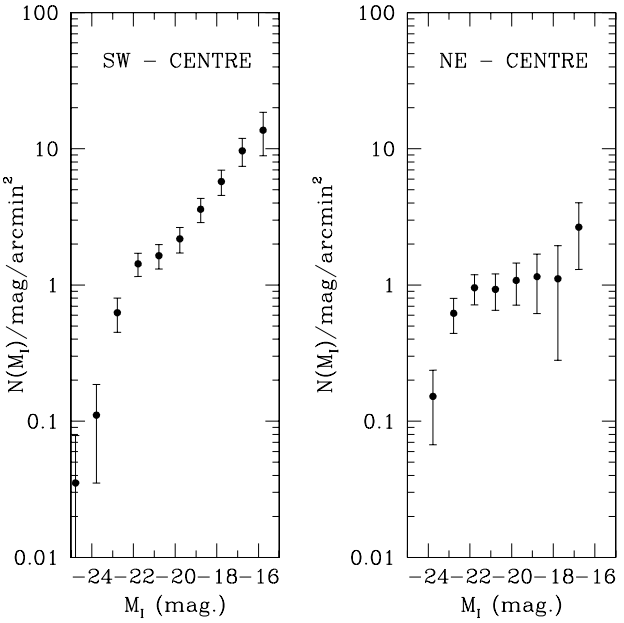

Figure 11. LFs for the central regions ($R_\mathrm{p} < 0.63$ Mpc or 2.75 arcmin) of the SW and NE clumps.

shows the distribution of redshifts centred on the SW peak and although two weak peaks occur near $cz = 53\,000$ and $80\,000\,\mathrm{km\,s^{-1}}$ there is no significant structure for $cz < 120\,000\,\mathrm{km\,s^{-1}}$.

Were a substantial number of redshifts available for i' fainter than 20, this possibility could possibly be sorted out.

Nevertheless, a distant cluster might show detectable differences in centre and in shape compared to the foreground cluster. To look for these effects, the galaxy sample was divided into bright ($M_I < -20.0$) and faint ($-16.0 > M_I \geq -20.0$) galaxies. Their values of L_I were converted from i' as described above, and isophotes were constructed using the Silverman (1986) adaptive kernel smoothing method. Fig. 13 shows bright galaxies in the left-hand panel. Both clumps show roughly circular isophotes and the peak of the SW clump is the higher. The isophotes for the faint galaxies in the right-hand panel differ. Here the NE clump is diminished relative to the SW clump, which is stronger. Using the faint galaxies, the peak of the SW clump is only slightly farther away from that of the NE clump along the axis joining them by $\approx 0.^{\circ}02$ or 0.3 Mpc.

The red sequence provides a second test for a distant cluster behind the SW clump. Such a cluster might have a typical I-band Schechter function ($\alpha = -1.27$, $M^* = -21.66$; e.g. Harsano & De Propis 2009). Assuming that the SW clump's LF is the same as that of NE plus the Schechter function, the distance modulus of the distant cluster should be larger by $\Delta DM \approx 3.2$ mag, or its distance modulus is 43.6, and $z \approx 0.85$. Although such a cluster lies

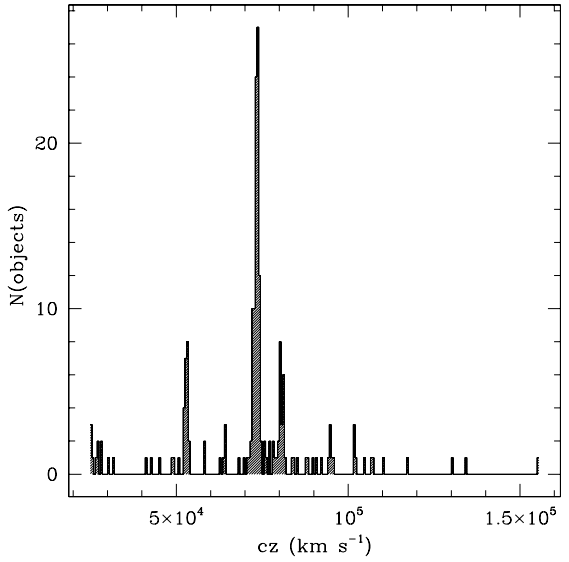

Figure 12. Redshifts of all galaxies centred on the SW clump. The strong peak near $z = 0.245$ comes from the Abell 2465 galaxies.

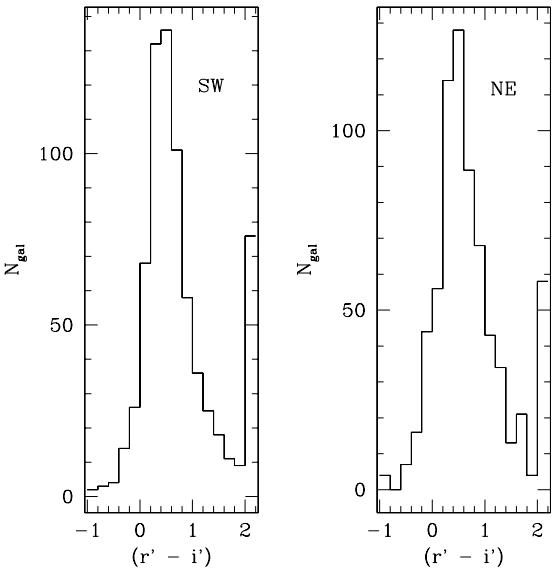

Figure 14. Histograms of the colour distributions for galaxies within 2.75 arcmin in the two clumps of Abell 2465 with apparent magnitudes $20.0 \leq i' \leq 24.4$.

beyond the currently available spectroscopy, at this z the change in K-corrections alone would make the distant cluster's $(r' - i')$ colour redder by about 1.3 mag (e.g. Fukugita et al. 1995). This effect is well illustrated by Gilbank et al. (2008) for composite clusters in $(R - z')$ for $z = 0.4$–0.9 which include evolutionary effects. This shifting of the red sequence could distort the shape of the red sequence of the SW region relative to the NE. One complication is that at increasing z, the blue sequence grows stronger and by $z = 0.85$ it lies near the low-redshift red sequence. However, the red sequence remains the stronger and should still be detectable.

To look for the shifted red sequence of a distant cluster, galaxies with $20.0 \leq i' \leq 24.4$ were binned in $(r' - i')$ for both clumps within 2.75 arcmin of their centres. As shown in Fig. 14, there is no apparent enhancement in $(r' - i')$ near 1.7 for the SW region compared to the NE. Applying the two-sample KS test (Press et al. 1992) supports the null hypothesis that the two samples are the same at the 99.8 per cent level, so a substantial cluster directly behind the SW clump seems unlikely. In the future, bluer colours would provide a more sensitive test.

In a test to fit different LFs to each clump, two approaches were employed. The first uses the prescription of Bingelli et al. (1988), also similar to Wilson et al. (1997). The E, S0 and spiral constituents are fitted by Gaussian functions and the dEs and dIrr follow Schechter functions. Here the fitting values of Jerjen & Tammann (1997) are used for the Gaussians and those of Bingelli et al. (1988) for the Schechter functions. The B-band magnitude zero-points were adjusted using mean $(B - I)$ colours for each galaxy type from Fukugita et al. (1995) and Smail et al. (1998) for the dEs. In Fig. 15, reasonable fits to the observed LFs of the two clumps are achieved. The relative proportions of the galaxy types given in Table 5 are similar for the two clumps, whilst the relative number of dEs is approximately five times higher in the SW clump compared to the NE. It should be noted that $\alpha = -1.35$ for the dE Schechter function is employed rather than the steeper $\alpha \approx -1.6$ to -2 predicted by ΛCDM.

The second approach uses the double Schechter function (Popesso et al. 2006) and others found that fits many clusters. Using published parameter values, these LFs do not agree well with those of Abell 2465. Other authors, e.g. Wolf et al. (2003) and Christlein et al. (2009), also found that simple LFs do not fit available data and obtain LFs similar in shape found here. They interpret the LFs as the sum of early types plus a rising late-type component composed of mostly faint blue star-forming galaxies.

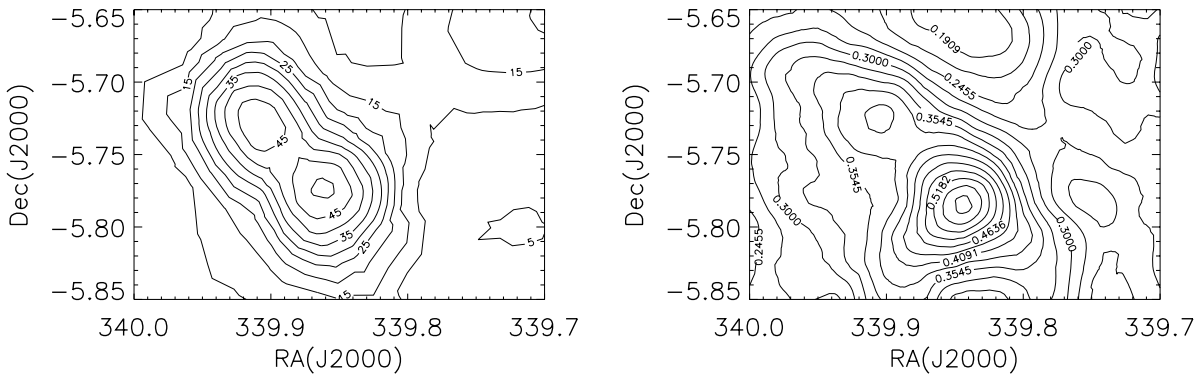

Figure 13. I-band isophotes for galaxies in the field of Abell 2465 constructed with the adaptive kernel method. Left-hand panel: all galaxies on the red sequence shown in Fig. 3 brighter than $M_I = -20.0$. Right-hand panel: all the fainter galaxies with $-16.0 > M_I \geq -20.0$. The dominance of the SW clump compared with the NE clump is notable. The scale of the isophotes is in arbitrary units.

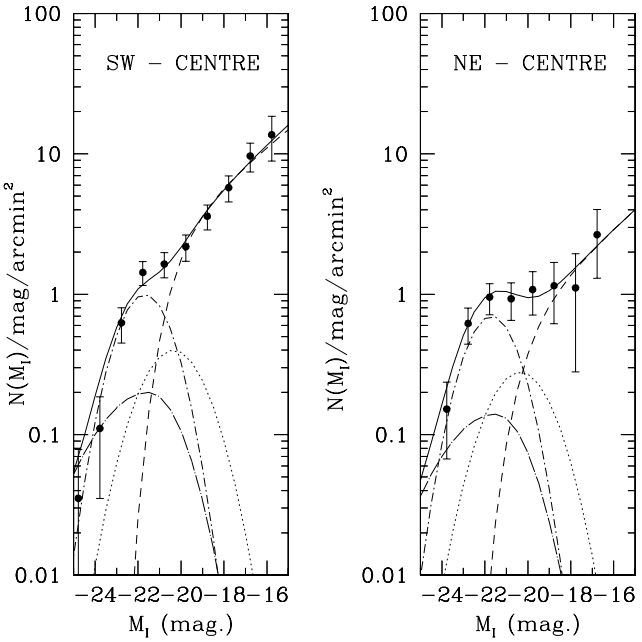

Figure 15. Fits to the LFs in Fig. 11 using the prescription given in Table 5. Long dash–dotted: ellipticals, short dash–dotted: S0s, dots: spirals and short dashes: dEs. The solid curve is the sum of the individual components.

Table 5. Relative normalization factors for the LFs and assumed $(B-I)$ colours.

	E	S0	Sp	dE
$(B-I)$	3.16	2.79	2.16	2.5
SW clump	0.5	2.5	1.0	4
NE clump	0.35	1.75	0.7	0.2

Independent of the fitting method, the outstanding feature is the difference in the numbers of faint galaxies following the dE Schechter function. There is an excess in the SW clump which is more luminous and slightly less massive, while the NE clump has fewer faint galaxies. Additional spectroscopic data are needed to establish the nature of the faint galaxies in the SW clump.

5 LIGHT PROFILES OF THE CLUMPS

The LF data are also employed to construct the light profiles. The apparent i' magnitudes were converted to absolute M_I Cousins magnitudes using the transformation in Section 4.2. The total light, $L_{\rm P}$, within circular apertures of radius $R_{\rm P}$ was measured starting from the cluster centres increasing the radius in 0.15-arcmin steps for projected radii. For $R_{\rm p} \leq 2.75$ arcmin circular areas were taken but for larger radii, the areas were corrected for the area of the missing segment that overlaps the other clump. The sums inside the aperture radii or growth curves give smoother curves than the projected luminosity.

The choice of the cluster centre affects results near the origin, but its influence decreases with radius. The BCGs and the X-ray centres of the NE clump differ by ∼22 arcsec. Therefore, the aperture profiles were constructed several times taking different centres within ±22 arcsec and averaged. This affects the central few points, but becomes negligible for radii larger than ∼0.45 arcmin, where the background's uncertainty dominates. The errors are estimated from the variance of the different counts and the counting statistics. The resulting curves are shown in Fig. 16 where they are compared with NFW growth curves for different concentration indices.

Several profile functions are known to fit galaxy clusters (e.g. Katgert et al. 2004). Although the purpose here is not to determine the optimal profile function, it is convenient to compare NFW profiles (Navarro et al. 1997) to the data in Fig. 16. The curves, assuming that $M/L \approx$ constant, are for different concentration parameters, c, computed using the formula for the projected mass:

$$M_{\rm p}(R) = g(c) M_{\rm v} \left[\frac{C^{-1}[1/(c\tilde{R})]}{|c^2\tilde{R}^2 - 1|^{1/2}} + \ln\left(\frac{c\tilde{R}}{2}\right)\right] \quad (8)$$

(Łokas & Mamon 2001), where $\tilde{R} = R/r_{\rm v}$, $M_{\rm v}$ is the virial mass,

$$g(c) = \frac{1}{\ln(1+c) - c/(1+c)}, \quad (9)$$

and $C^{-1}(x) = \cos^{-1}(x)$ for $R > r_s$ and $\cosh^{-1}(x)$ if $R < r_s$. The best-fitting NFW profile was found using the KS test (Kreyszig 1991; Press et al. 1992) on the projected growth curve in Fig. 16. Note that data are displayed in a semilog plot whilst the KS test is done linearly. In these determinations, the spectroscopic values of r_{200} were used. SW follows curves with $c = 4 \pm 2$ and NE lies closer to $c = 10 \pm 5$. However, although the single NFW profile fits the NE region relatively well, agreement is poorer for the SW clump, particularly near $R_{\rm p}/r_{200} \approx 0.3$ where the data rise compared to the nearby smooth NFW curves for different values of c.

Viewing Fig. 1, this rise should result from the bright BCG complex near the centre of the SW clump. Consequently, a more complicated composite profile containing a bright core yields a better fit. However, which combination of profiles is the best is difficult to decide with the present data. One possibility shown in Fig. 17 is to add two NFW profiles, one with $c = 120$ which gives a sharp core and the other with $c = 1.0$ which produces an extended outer region. This confirms that the SW clump is more centrally concentrated as it is also in X-rays.

Measurements of c based on mass give somewhat different values for c. Katgert et al. (2004) found $c = 4^{+2.7}_{-1.5}$ from a cluster ensemble, while Biviano & Girardi (2003) found $c \approx 5.6$ and Carlberg et al. (1996) obtained $c \approx 4$. Thus, c for the SW component might lie within the normal range except for its core, but for NE clump c is larger. Theoretical values of c based on the buildup of dark haloes in CDM models (e.g. Zhao et al. 2003) agree with the lower value of c, so the higher value for NE is difficult to explain, although the value of c depends on the accretion rate of the cluster.

The value of c does depend on the choice of r_{200}. However, to achieve a fit resulting in $c = 5$ for the NE clump requires lowering r_{200} to half its spectroscopic value, or 6σ. If the mass distributions in the subclusters of Abell 2465 differ from those found here for light, this may imply that they may have been disturbed by the merging process.

As seen in Fig. 16, the total luminosities are $L_I = 4.4 \pm 0.6 \times 10^{12}\,{\rm L}_\odot$ for SW and $L_I = 3.8 \pm 0.7 \times 10^{12}\,{\rm L}_\odot$ for NE. Using the mean of the virial and X-ray masses gives mass-to-light ratios (M/L) in the I band of $M/L = 84 \pm 12$ and 112 ± 20, respectively. Noting that $(R-I) \approx 0.7$ for early-type galaxies, in the R band (Fukugita et al. 1995), $\Upsilon_R \approx 1.9\Upsilon_I$ so the mass ratios lie marginally within the range for single galaxy clusters which is $\Upsilon_R = 200 \pm 50$ in the R band (Binney & Tremaine 2008). The more massive NE clump has the higher M/L while the SW clump has the more concentrated core.

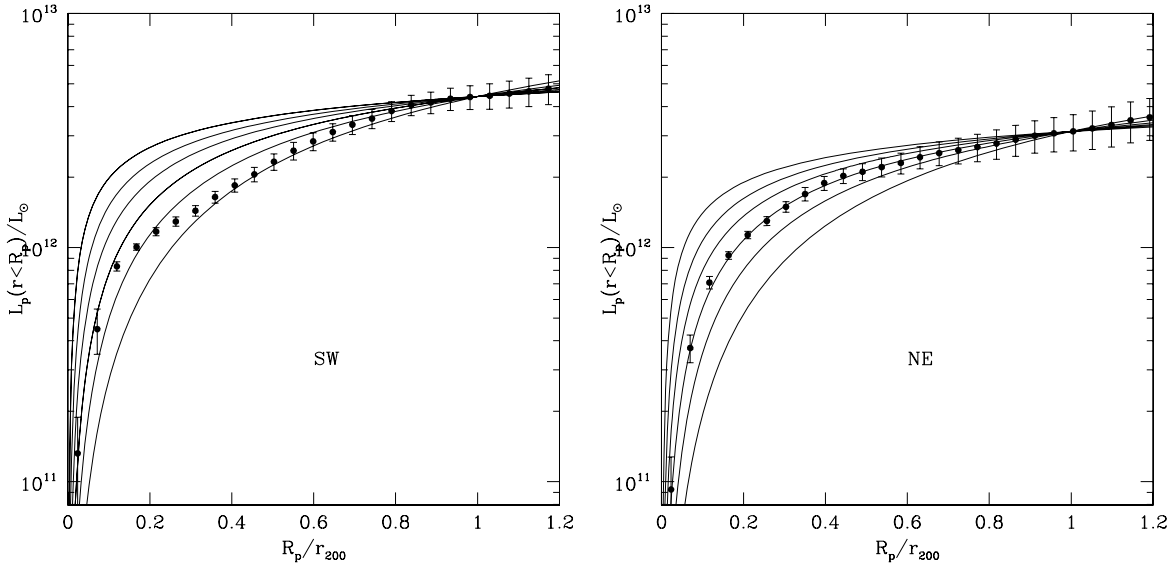

Figure 16. The total projected light inside radius R_p for the two clumps of Abell 2465 and their errors. Curves for NFW profiles with different concentration indices are superimposed; from top to bottom: $c = 100$, 40, 20, 10, 5 and 2. SW has $L_p = 4.4 \times 10^{12}\,L_\odot$ at $r_{200} = 1.21$ Mpc and fits with $c \approx 4$, while NE has $L_p = 3.8 \times 10^{12}\,L_\odot$ at $r_{200} = 1.25$ Mpc with $c \approx 10$.

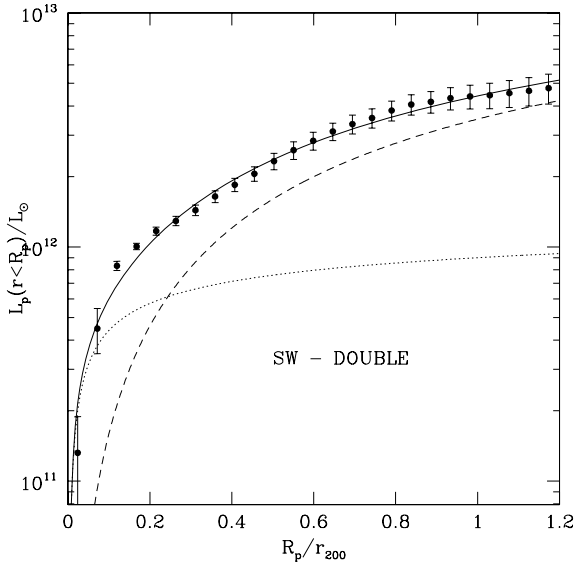

Figure 17. Fit to the growth curve of the SW clump of Abell 2465 data given in Fig. 16 using the double model discussed in the text. The dashed curve is for an NFW profile with $c = 1.0$ and the dotted curve is for $c = 120$. The solid curve is their sum.

6 DISCUSSION

The mass ratio near unity indicates that the components of Abell 2465 are undergoing a major merger. However, the question that needs to be answered is whether Abell 2465 is beginning the merger or if a collision has already occurred. The main properties of this double galaxy cluster have both some normal and some unusual properties. On one hand, the masses and virial radii are similar to single clusters as are their velocity dispersion anisotropies. On the other hand, the differences in their LFs, M/L and the presence of many star-forming galaxies located between the two clumps offer additional clues to the processes involved in their earlier interaction which tend to favour the past collision hypothesis.

6.1 Separation of the baryonic and collisionless components

After pericentric passage in galaxy cluster collisions, a generic result is that the highly heated baryonic gas is temporarily retarded relative to the collisionless dark matter and galaxies with the outcome that the X-ray centres are closer together than the dark matter centres. The separation is expected to be smaller for nearly equal mass clusters than it is for higher mass ratios (e.g. Tormen, Moscardini & Yoshida 2004; Poole et al. 2006). The gas cools and re-merges with the collisionless components at later times. These effects are observed in several recent ($\tau_{\rm coll} \lesssim 0.1$–$0.3$ Gyr) collisions with higher mass ratios, notably 1E 0657−56 (Clowe et al. 2006), Abell 2146 (Russell et al. 2010) and MACS J0025.4−1222 (Bradač et al. 2008b), where X-ray emission is between the dark matter clumps as revealed by lensing and the galaxies.

For Abell 2465, the X-ray and BCG centres are shown in Table 1. Displacements occur along the axis in Fig. 9 joining the two clumps, putting the X-ray peaks between the BCGs. These amount to 22.1 arcsec (85 kpc) for the NE and 2.4 arcsec (9 kpc) for the SW. The isophotal peaks from the galaxies in Fig. 13 are more unreliable. These change by $\sim\pm25$ arcsec depending on whether different magnitude ranges or galaxy numbers are used to construct the contours. These place the centres of the galaxy distributions near or slightly inside the X-ray peaks along the axis. Relative to the 5.5 arcmin separating the clumps, displacements are small compared to the above colliding clusters. Thus, while the separation of the components is consistent with a past collision, using the X-ray and BCG locations, their small separations suggest that the NE and SW subclusters have not recently collided.

6.2 Nature of the interaction

The radial infall model (Beers et al. 1982) has often been used as a first approximation to study head-on collisions, despite its obvious limitations, including neglect of dynamical friction and gas dynamics. It is an analytic solution based on the Einstein–de Sitter cosmological model and has been employed by many investigators (e.g. Gregory & Thompson 1984; Beers et al. 1991; Scodeggio

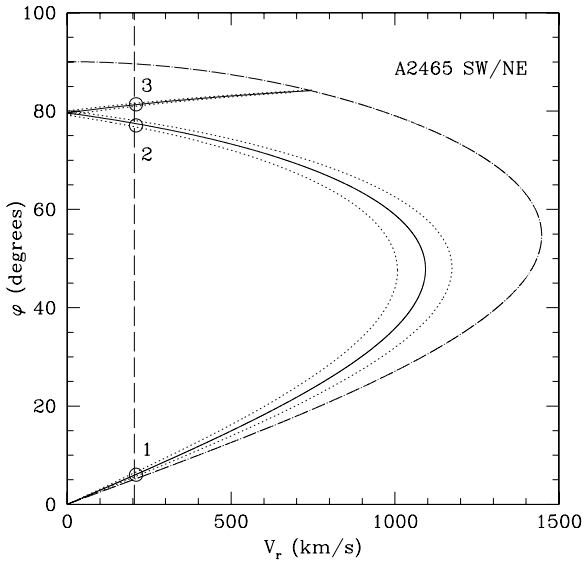

Figure 18. Radial infall model solutions for Abell 2465. The rightmost (dot–dashed) curve is the limit of bound solutions; solutions to its right are unbound. Solutions for $8 \times 10^{14}\,\mathrm{M}_\odot$ (solid) and 9×10^{14} and $7 \times 10^{14}\,\mathrm{M}_\odot$ (dotted) lie on either side. The vertical dashed line shows the measured value of V_r and circles mark the three possible solutions indicated by the numbers.

et al. 1995; Colless & Dunn 1996; Mohr & Wegner 1997; Donnelly et al. 2001; Yuan et al. 2005; Hwang & Lee 2009) and will only be outlined here. Briefly, two mass points with total mass, M, following radial orbits are assumed and R, their separation; V, the relative velocity; and t, the time are given parametrically in terms of the development angle, η. The masses coincide at pericentre when $\eta = 0, 2\pi, \ldots$ and are at apocentre when $\eta = \pi, 3\pi, \ldots$. The solution requires M, the projected distance, R_p, and, t_0, the system's age, usually set equal to the age of the Universe. Since the inclination angle φ is unknown, the system of equations can be written in terms of $R_\mathrm{p} = R\cos\varphi$, the projected distance between the masses, radial velocity difference, $V_\mathrm{r} = V\sin\varphi$ and M. The bound case for the two masses obeys $V_\mathrm{r}^2 \leq 2GM\,\sin^2\varphi\,\cos\varphi$ and three solutions are possible: two collapsing or ingoing and one expanding or outgoing. The M and V_r of Section 3 place the cluster pair within the bound region, and hence the unbound case is not considered.

Using $M = 8 \pm 1 \times 10^{14}\,\mathrm{M}_\odot$, $R_\mathrm{p} = 1.265$ Mpc and 10.895 Gyr, the age of the universe at $z = 0.245$, one can construct curves of the solutions within the permitted regions shown in Fig. 18.

With $V_\mathrm{r} = 205\,\mathrm{km\,s^{-1}}$ the three possible solutions are as follows: (1) $\eta = 5.17$ rad, $\varphi = 5.95$, $R = 1.31$ Mpc, $R_\mathrm{m} = 4.53$ Mpc and $V = -1978\,\mathrm{km\,s^{-1}}$; (2) $\eta = 3.53$ rad, $\varphi = 77.5$, $R = 6.01$ Mpc, $R_\mathrm{m} = 6.07$ Mpc and $V = -210\,\mathrm{km\,s^{-1}}$ and (3) $\eta = 2.68$ rad, $\varphi = 81.3$, $R = 8.59$ Mpc, $R_\mathrm{m} = 8.81$ Mpc and $V = +208\,\mathrm{km\,s^{-1}}$. Intuition suggests that either solution (2) or (3) might be preferable given the low observed value for V_r, placing the two clumps near the apocentre, but further data are required.

Numerical simulations provide a better time-scale estimate of galaxy clusters, including galaxies, baryonic and dark matter. The colliding models typified by e.g. Roettiger et al. (1996, 1997), Ritchie & Thomas (2002) and Poole et al. (2006, 2008), while idealized and differing in details, predict similar effects in the collisions and suggest shorter times between collisions than what the radial infall model predicts.

Published merger models focus on X-ray data and employ several simplifications, including e.g. assumed initial density profiles, velocities and spherical symmetry. Nevertheless, three effects common to the models are important for this study. (1) Head-on and off-centre simulations generally merge soon after their second crossing, indicating that the two subclusters in Abell 2465 have collided at most once or are merging for the first time. (2) The gas components' temperatures spike when the two centres cross and cool rapidly. Following Ritchie & Thomas (2002), the collision of $M = 4 \times 10^{14}\,\mathrm{M}_\odot$ equal masses, close to that estimated for Abell 2465, the gas temperature reaches ∼10 keV and cools to ∼3 keV in about 3–4 Gyr as the clumps separate to apocentre and begin reconverging. The temperatures of Section 3.3 will be consistent with this time-scale if the cluster is in the post-impact stage, but cannot be used to prove the physical state of the merger. (3) The collision produces an expanding impact disc of gas as two clusters pass through each other which breaks into two sections continuing outwards with the main masses. Zu Hone, Lamb & Ricker (2009) have discussed ring formation. The dark matter components pass through each other and the core regions are not disrupted.

Tormen et al. (2004) analysed the evolution of merging galaxy cluster satellites from hydrodynamical N-body simulations including dark matter and baryonic gas. They fitted the statistics of collisions including orbital properties, velocity dispersions, gas temperatures, etc., as a function of the satellite and the main cluster pre-merger mass ratio, $m_\mathrm{v}/M_\mathrm{v}$. For $m_\mathrm{v}/M_\mathrm{v} \approx 0.9$, ∼2 Gyr is required to reach apocentre. Consequently, this and the temperature ageing indicate that the time since the collision is of the order $\tau \sim$ 2–4 Gyr.

The cluster light profiles and LFs provide additional clues to the interaction of the two components of Abell 2465. The SW clump has a sharper core in both the visual and X-rays as well as more faint galaxies shown in Figs 11 and 13. The two well-studied cluster collisions involving recent impacts, 1E 0657−56 and Abell 2146 (Clowe et al. 2006; Russell et al. 2010), have lower mass ratios of $m_\mathrm{v}/M_\mathrm{v} \approx 0.1$ and 0.3, respectively. Both exhibit a relatively dense 'bullet' emerging from a more extended 'target' and are near their pericentres, having collided $\tau \sim 0.1$–0.3 Gyr ago, compared to $\tau \sim$ 3 Gyr for the cooler Abell 2465 now near the apocentre. By analogy with these two objects, one identifies the SW clump with its sharper optical and X-ray core as the bullet and the more extended NE clump as the target. The presence of the 1.4-GHz radio source and its higher mass further imply that the NE clump is the primary.

Although cluster cores are not disrupted, the outer regions can be modified. The published simulations show complex behaviour of the collisionless component. Bekki (1999) and Roettiger, Loken & Burns (1993) demonstrated that the distribution of dark matter in the secondary expands after the collision. Using the simple impact approximation (Binney & Tremaine 2008), energy changes accompanied by mass-loss of the impacting systems occur. Intuitively, one expects core regions to contract as they meet while the outer layers of the clusters expand (e.g. Aguilar & White 1985; Funato & Makino 1999). Some of the off-centre models (e.g. Ricker & Sarazin 2001; Poole et al. 2006) show that when the secondary core reaches apocentre and turns around, there is a significant displacement of the cluster's outer region which is assisted by a gravitational slingshot similar to a trailing tidal trail. Thus, the SW clump might be expected to be surrounded by more debris than the NE clump which accounts for its excess of faint galaxies.

6.3 On the star-forming components

Previous investigations have found inconclusive results for different cluster pairs regarding star formation. Hwang & Lee (2009)

found enhanced star formation activity between the subclusters of Abell 168 which they concluded had passed through each other and none in Abell 1750 which may be in an early stage of merging. Rawle et al. (2010) have found significant star formation in the bullet cluster using *Herschel*. Caldwell & Rose (1997) reported enhanced star forming in interacting clusters as did Cortese et al. (2004) for Abell 1367, Ferrari et al. (2005) for Abell 3921 and Johnston-Hollitt et al. (2008) for Abell 3125/28, but Tomita et al. (1996) and De Propis et al. (2004) found no correlation for blue galaxies and mergers. Ma et al. (2010) have described MACS J0025.4−1225, which has several features in common with Abell 2465, as a post-major merger. They found enhanced numbers of star-forming galaxies which they interpret to have been produced by the merger. The emission-line galaxies in Abell 2465, however, lend weight to the hypothesis that cluster mergers enhance star formation.

It has always been difficult to pin down the process or combination of processes leading to star formation in galaxies. Bekki (1999) found that the time-dependent tidal gravitational field is an important effect that can trigger starburst galaxies in mergers. Martig & Bournaud (2008) also found that tidal fields in merging dense cosmological structures and the outskirts of galaxy clusters can induce star formation. The presence of apparently distorted star-forming galaxies with no detected companions in the clusters could be consistent with this mechanism.

7 CONCLUSIONS

Spectroscopic and photometric observations of the double galaxy cluster Abell 2465 are presented. There are five main conclusions that can be drawn.

(1) Concerning the cluster dynamics, the virial masses of the two subclusters are found from fuzzy clustering, which is used to estimate the probability of a galaxy's membership in each clump, with the result that $M_{\rm v} = 4.0 \pm 0.8 \times 10^{14}\,{\rm M}_{\odot}$ for the NE member and $M_{\rm v} = 3.8 \pm 0.8 \times 10^{14}\,{\rm M}_{\odot}$ for the SW member and the virial radii are $r_{200} = 1.21 \pm 0.11$ and 1.24 ± 0.09 Mpc for NE and SW, respectively. The masses compare well with those from X-ray scaling relations that also give temperatures of 4.1 ± 0.3 and 3.75 ± 0.2 keV, respectively. The velocity difference between the two subclusters is found to be $\Delta V = 205 \pm 149\,{\rm km\,s^{-1}}$ which confirms that they are related. Measurement of the clusters' velocity dispersions with radius assuming spherical symmetry indicates that the anisotropy parameter, β, is low.

(2) There is an excess of star-forming galaxies showing emission lines. Of cluster members observed spectroscopically in Fig. 8, 37 per cent have detectable Hα emission. These have the properties of star-forming galaxies. There are more emission-line objects in the SW clump than in the NE clump and there appears to be more emission-line galaxies than non-emission between the two clumps. This does not seem to be explained by a selection bias. There is no evidence for strong AGN activity in Abell 2465. This number of emission-line objects between the clump centres is unusual when compared to single galaxy clusters.

(3) The r' and i' magnitudes show well-defined red sequences in each subcluster. The LFs determined within the central 0.6 Mpc of each clump indicate a normal mixture of galactic types. However, the SW region has more galaxies fainter than $M_I = -20.0$ than its NE companion. This could result from their collision or otherwise would suggest different formation histories. The possibility of a background cluster needs to be further checked.

(4) The light profiles of both components measured as growth curves were fitted using NFW profiles. The NE clump is fitted with a somewhat high concentration parameter $c = 10$, although this depends on the adopted virial radius. The SW clump is fitted rather badly with $c = \sim 4$ and needs a profile with a more compact core. A better fit is a sharp core ($c = 120$) surrounded by an extended outer region ($c = 1.0$). This is consistent with Fig. 6 and published *ROSAT* data showing that the X-ray core radii differ with $r_{\rm c}$ of NE, being about three times larger than that of the SW and indicates that SW has a CC. The derived I-band M/L are $\Upsilon_I = 84 \pm 12$ and 112 ± 20 which puts them in the normal range for galaxy clusters.

(5) A consistent picture of the collision of the Abell 2465 components is discussed. It is possible that the pair collided 2–4 Gyr ago and are now near maximum separation. The small displacements of the dark matter and baryonic matter as judged by the X-ray data and distribution of the galaxies are consistent with their re-merging after the collision. The high percentage of emission-line galaxies in the spectroscopic sample may be a consequence of the collision and is the strongest argument for a past interaction, but this might also be the case if the merger is just starting and interaction occurs along the interface between the two clusters. More models that include the dynamics of the galaxies would be helpful.

A weak lensing study of the two components of Abell 2465 is underway.

ACKNOWLEDGMENTS

Many of the galaxy spectra were obtained through the Service Observing Programme of AAT and I wish to express my gratitude. The imaging observations used in this paper were based on observations obtained with MegaPrime/MegaCam, a joint project of CFHT and CEA/DAPNIA, at the CFHT which is operated by the National Research Council (NRC) of Canada, the Institut National des Science de l'Univers of the Centre National de la Recherche Scientifique (CNRS) of France and the University of Hawaii. This work is based in part on data products produced at TERAPIX and the Canadian Astronomy Data Centre as part of the Canada–France–Hawaii Telescope Legacy Survey, a collaborative project of NRC and CNRS. I thank the Canadian TAC for granting the time and the QSO team for obtaining the imaging data. This research has made use of the NASA/IPAC Extragalactic Database (NED) which is operated by the Jet Propulsion Laboratory, California Institute of Technology, under contract with the National Aeronautics and Space Administration. Many thanks to Dr J. J. Mohr and Mr Dane Owen for help on the MDM photometry, Mr R. E. Johnson for discussions and Dr. Heinz Andernach for comments.

REFERENCES

Aguilar L., White S. D. M., 1985, ApJ, 295, 374
Anderberg M. R., 1973, Cluster Analysis for Applications. Academic Press, New York
Angus G. W., McGaugh S. S., 2008, MNRAS, 383, 417
Angus G. W., Famaey B., Diaferio A., 2010, MNRAS, 402, 395
Bagchi J., Durret F., Neto G. B. L., Paul S., 2006, Sci, 314, 791
Balogh M. et al., 2004, MNRAS, 348, 1355
Beers T. C., Geller M. J., Huchra J. P., 1982, ApJ, 257, 23
Beers T. C., Gebhardt K., Forman W., Huchra J. P., Jones C., 1991, AJ, 102, 1581
Bekki K., 1999, ApJ, 510, L15
Bertin E., 2009, SExtractor v2.5 User's Manual, http://astroa.physics.metu.edu.tr/MANUAL/sextractor

Bertin E., Arnouts S., 1996, A&AS, 117, 393
Bingelli B., Sandage A., Tammann G. A., 1988, ARA&A, 26, 509
Binney J., Merrifield M., 1998, Galactic Astronomy. Princeton Univ. Press, Princeton, p. 53
Binney J., Tremaine S., 2008, Galactic Dynamics. Princeton Univ. Press, Princeton, p. 655
Biviano A., Girardi M., 2003, ApJ, 585, 205
Blanton M. R., Roweis S., 2007, AJ, 133, 734
Blanton M. R. et al., 2003, ApJ, 592, 819
Bonafede A., Giovannini G., Feretti L., Govoni F., Murgia M., 2009, A&A, 494, 429
Bradač M. et al., 2008a, ApJ, 681, 187
Bradač M., Allen S. W., Treu T., Ebeling H., Massey R., Morris R. G., van den Linden A., Applegate D., 2008b, ApJ, 687, 959
Brownstein J. R., Moffat J. W., 2007, MNRAS, 382, 29
Caldwell N., Rose J. A., 1997, AJ, 113, 492
Cappellari M. et al., 2006, MNRAS, 366, 1126
Carlberg R. G., Yee H. K. C., Ellingson E., Abraham R., Gravel P., Morris S., Pritchet C. J., 1996, ApJ, 462, 32
Chen Y., Reiprich T. H., Böhringer H., Ikebe Y., Zhang Y.-Y., 2007, A&A, 466, 805
Chionis T. S., Gaskell C. M., 2008, AJ, 135, 264
Christlein D., Zabludoff A. I., 2003, ApJ, 591, 764
Christlein D., Gawiser E., Marchesini D., Padilla N., 2009, MNRAS, 400, 429
Chung S. M., 2010, BAAS, 42, 601
Clowe D., Bradač M., Gonzales A. H., Markevitch M., Randall S. W., Jones C., Zaritsky D., 2006, ApJ, 648, 109
Colless M., Dunn A. M., 1996, ApJ, 458, 435
Condon J. J., Cotton E. W., Griesen E. W., Yin Q. F., Perley R. A., Taylor G. B., Broderick J. J., 1998, AJ, 115, 1693
Cortese L., Gavazzi G., Boselli A., Iglesias-Paramo J., Carrasco L., 2004, A&A, 425, 429
De Lorenci V. A., Faundez-Abans M., Pereira J. P., 2009, A&A, 503, 1
De Propis R. et al., 2004, MNRAS, 351, 125
Diaferio A., 1999, MNRAS, 309, 610
Dickey J. M., Lockman F. J., 1990, ARA&A, 28, 215
Donelly R. H., Forman W., Jones C., Quintana H., Ramirez A., Churazov E., Gilfanov M., 2001, ApJ, 562, 254
Dressler A., Schechtman S. A., 1988, ApJ, 95, 985
Farrar G. R., Rosen R. A., 2006, Phys. Rev. Lett., 98, 1302
Fasano G., Franceschini A., 1987, MNRAS, 225, 155
Feretti L., 2002, in Pramesh Rao A., Swarup G., Gopal-Krishna, eds, Proc. IAU Symp. 199, The Universe at Low Radio Frequencies. Kluwer, Dordrecht, p. 133
Ferrari C., Maurogordato S., Cappi A., Benoist C., 2003, A&A, 399, 813
Ferrari C., Benoist C., Maourogordato S., Cappi A., Slezak E., 2005, A&A, 430, 19
Fukugita M., Shimasaku K., Ichikawa T., 1995, PASP, 107, 945
Funato Y., Makino J., 1999, ApJ, 511, 625
Gan G., Ma C., Wu J., 2007, Data Clustering, Theory, Algorithms, and Applications. SIAM, Philadelphia, PA
Geller M. J., Beers T. C., 1982, PASP, 94, 421
Gilbank D. G., Yee H. K. C., Ellingson E., Gladders M. D., Loh Y.-S., Barrientos L. F., Barkhouse W. A., 2008, ApJ, 673, 742
Girardi M., Giuricin G., Mardirossian F., Mezzetti M., Boschin W., 1998, ApJ, 505, 74
Girardi M., Barrena R., Boschin W., Ellingson E., 2008, A&A, 491, 379
Goto T. et al., 2005, ApJ, 621, 188
Gregory S. A., Thompson L. A., 1984, ApJ, 286, 422
Haines C. P., Smith G. P., Egami E., Okabe N., Takada M., Ellis R. S., Moran S. M., Umetsu K., 2009, MNRAS, 396, 1297
Hallman E. J., Markevitch M., 2004, ApJ, 610, L81
Hansen S. H., Piffaretti R., 2007, A&A, 476, L37
Harsano D., De Propis R., 2009, Astron. Nachr., 330 937
Hayashi E., White S. D. M., 2006, MNRAS, 370, L38
Heiderman A. et al., 2009, ApJ, 705, 1433
Heisler J., Tremaine S., Bahcall J. N., 1985, ApJ, 298, 8
Holwerda B. W., 2005, Source Extractor for Dummies, preprint (astro-ph/0512139)
Höppner F., Klawonn F., Kruse R., Runkler T., 1999, Fuzzy Cluster Analysis: Methods for Classification, Data Analysis, and Image Recognition. Wiley, Chichester
Host O., 2009, Nuclear Phys. B, 194, 111
Host O., Hansen S. H., Piffaretti R., Morandi A., Ettori S., Kay S. T., Valdarnini R., 2009, ApJ, 690, 358
Hwang H. S., Lee M. G., 2009, MNRAS, 397, 2111
Jee M. J. et al., 2007, ApJ, 661, 728
Jerjen H., Tammann G. A., 1997, A&A, 321, 713
Johnston-Hollitt M., Sato M., Gill J. A., Fleenor M. C., Brick A.-M., 2008, MNRAS, 390, 289
Jordi K., Grebel E. K., Ammon K., 2006, A&A, 430, 339
Kalberla P. M., Burton W. B., Hartmann D., Arnal E. M., Bajaja E., Morras R., Pöppel W. G. L., 2005, A&A, 440, 775
Katgert P., Biviano A., Mazure A., 2004, ApJ 600, 657
Kaufman L., Rousseeuw P. J., 2005, Finding Groups in Data. Wiley, Hoboken
Kaufmann G. et al., 2003, MNRAS, 346, 1055
Kewley L. J., Dopita M. A., Sutherland R. S., Heisler C. A., Trevena J., 2001, ApJ, 556, 121
Kreyszig E., 1991, Statistische Methoden und ihre Anwendungen, 7. Auflage, Vandenhoek & Ruprecht, Göttingen
Kriessler J. R., Beers T. C., 1997, AJ, 113, 80
Kubo J. M., Stebbins A., Annis J., Dell Antonio I. P., Lin H., Frieman J. A., 2007, ApJ, 671, 1466
Landolt A. U., 2009, AJ, 137, 4186
Leauthaud A. et al., 2007, ApJS, 172, 219
Łokas E. L., Mamon G. A., 2001, MNRAS, 321, 155
Ma C.-J., Ebeling H., Marshall P., Schrabback T., 2010, MNRAS, 406, 121
McCracken H. J., Le Fevre O., Brodwin M., Foucaud S., Lilly S. J., Crampton D., Mellier Y., 2001, A&A, 376, 756
Madgwick D. S. et al., 2002, MNRAS, 333, 133
Markevitch M., Vikhlinin A., 2007, Phys. Rep, 443, 1
Martig M., Bournavd F., 2008, MNRAS, 385, L38
Mastropietro C., Burkert A., 2008, MNRAS, 389, 967
Maurogordato A. et al., 2008, A&A, 481, 593
Merritt D., 1985, AJ, 90, 1027
Miyamoto S., Ichihashi H., Honda K., 2008, Algorithms for Fuzzy Clustering Methods in c-Means Clustering with Applications. Springer-Verlag, Berlin
Mohr J. J., Wegner G., 1997, AJ, 114, 25
Natarajan P., Zhao H., 2008, MNRAS, 389, 250
Navarro J. F., Frenk C. S., White S. D. M., 1997, ApJ, 490, 493
O'Hara T. B., Mohr J. J., Bialek J. J., Evrard A. E., 2006, ApJ, 639, 64
Okabe N., Umetsu K., 2008, PASJ, 60, 345
Orrú E., Murgia M., Feretti L., Govoni F., Brunetti G., Giovannini G., Giardi M., Setti G., 2007, A&A, 467, 943
Osipkov L. P., 1979, PAZh, 5, 77
Penny S. J., Conseliche C. J., De Rijcke S., Held E. V., Gallagher J. S., III, O'Connell R. W., 2010, MNRAS, 410, 1076
Perlman E., Horner D. J., Jones L. R., Scharf C. A., Ebeling H., Wegner G., Malkan M., 2002, ApJS, 140, 265
Pinkney J., Roettiger K., Burns J. O., Bird C. M., 1996, ApJS, 104, 1
Planelles S., Quilis V., 2009, MNRAS, 399, 410
Pointecouteau E., Silk J., 2005, MNRAS, 364, 654
Pointecouteau E., Arnaud M., Pratt G. W., 2005, A&A, 435, 1
Poole G. B., Fardal M. A., Babul A., McCarthy I. G., Quinn T., Wadsley J., 2006, MNRAS, 373 881
Poole G. B., Babul A., McCarthy I. G., Sanderson A. J. R., Fardal M. A., 2008, MNRAS, 391, 1163
Popesso P., Biviano A., Böhringer H., Romaniello M., Voges W., 2005, A&A, 433, 431
Popesso P., Biviano A., Böhringer H., Romaniello M., 2006, A&A, 445, 29
Press W. H., Teukolsky S. A., Vetterling W. T., Flannery B. P., 1992, Numerical Recipes in Fortran, 2nd edn. Cambridge Univ. Press, Cambridge

Ramella M. et al., 2007, A&A, 470, 39
Rawle T. D. et al., 2010, A&A, 518, 14
Raymond J. C., Smith B. W., 1977, ApJS, 35, 419
Reiprich T., Böhringer H., 2002, ApJ, 567, 740
Ricker P. M., 1998, ApJ, 496, 670
Ricker P. M., Sarazin C. L., 2001, ApJ, 561, 621
Rines K., Geller M. J., Kurtz M. J., Diaferio A., 2005, AJ, 130, 1482
Ritchie B. W., Thomas P. A., 2002, MNRAS, 329, 675
Roettiger K., Loken C., Burns J., 1993, ApJ, 407, L53
Roettiger K., Loken C., Burns J. O., 1996, ApJ, 473, 651
Roettiger K., Loken C., Burns J. O., 1997, ApJS, 109, 307
Russell H. R., Sanders J. R., Fabian A. C., Baum S. A., Donahue M., Edge A. C., McNamara B. R., O'Dea C. P. O., 2010, MNRAS, 406, 1721
Rykoff E. S. et al., 2008, MNRAS, 387, 28
Sakelliou I., Ponman T. J., 2004, MNRAS, 351, 1439
Salvador-Solé E., Sanromà M., González-Casado G., 1993, ApJ, 402, 398
Sanderson A. J. R., Ponman T. J., Finoguenov A., Lloyd-Davies E. J., 2003, MNRAS, 340, 989
Sarazin C. L., 1986, Rev. Modern Phys., 58, 1
Sato M., Sato Y., Jain L. C., 1997, Fuzzy Clustering Models and Applications. Physica-Verlag, Heidelberg
Schechter P., 1976, ApJ, 203, 297
Schmidt F., Vikhlinin A., Hu W., 2009, Phys. Rev. D, 80, 083505-1
Scodeggio M., Solanes J. M, Giovanelli R., Haynes M. P., 1995, ApJ, 444, 41
Serna A., 1996, J. Comput. Phys., 129, 30
Shan H. Y., Qin B., Fort B., Tao C., Wu X.-P., 2010, MNRAS, 406, 1134
Silverman B. W., 1986, Density Estimation for Statistics and Data Analysis. Chapman and Hall, London
Skillman S. W., Hallman E. J., O'Shea B. W., Burns J. O., Smith B. D., Turk M. J., 2010, ApJ, submitted (arXiv:1006.3559)
Slee O. B., Roy A. L., Murgia M., Andernach H., Ehle M., 2001, AJ, 122, 1172
Smail I., Edge A. C., Ellis R. S., Blandfored R. D., 1998, MNRAS, 283, 124
Springel V., Farrar G. R., 2007, MNRAS, 380, 911
Tanaka N., Furuzawa A., Miyoshi J., Tamura T., Takata T., 2010, PASJ, 62, 743
Takizawa M., 2000, ApJ, 532, 183
Takizawa M., Nagino R., Matsushita K., 2010, PASJ, 62, 951
Thomas P. A. et al., 1998, MNRAS, 296, 1061
Tomita A., Nakamura F. E., Tukata T., Nakanishi K., Takeuchi T., Ohta K., Yamada T., 1996, AJ, 111, 42
Tonry J., Davis M., 1979, AJ, 84 1511
Tormen G., Moscardini L., Yoshida N., 2004, MNRAS, 350, 1397
Tremaine S., Gunn J. E., 1979, Phys. Rev. Lett., 42, 407
Tully R. B., 1980, ApJ, 237, 390
van Weeren R. J., Intema H. T., Röttgering H. J. A., Clarke T. E., 2009, A&A, 508, 1269
Vikhlinin A., McNamara B. R., Forman W., Jones C., Quintana H., Hornstrup A., 1998, ApJ, 502, 558
Wegner G., Grogin N. A., 2008, AJ, 136, 1
Wilms J., Allen A., McCray R., 2000, ApJ, 542, 914
Wilson G., 2003, ApJ, 585, 191
Wilson G., Smail I., Ellis R. S., Couch W. J., 1997, MNRAS, 284, 915
Wolf C., Meisenheimer K., Rix H.-W., Borch A., Dye S., Kleinheinrich M., 2003, A&A, 401, 73
Yan R., Newman J. A., Faber S. M., Konidaris N., Koo D., Davis M., 2006, ApJ, 648, 281
Yuan Q., Yan P., Ying Y., Zhou X., 2005, Chinese J. Astron. Astrophys., 5, 126
Zhao D. H., Jing Y. P., Mo H. J., Börner G., 2003, ApJ, 597, L9
Zu Hone J., Markevitch M., 2009, in Ok S. H., Wilcots E., eds, AIP Conf. Proc. Vol. 1201, Cluster Core Heating from Merging Subclusters. Am. Inst. Phys., New York, p. 383
Zu Hone J. A., Lamb D. Q., Ricker P. M., 2009, ApJ, 696, 649

This paper has been typeset from a TEX/LATEX file prepared by the author.